FMA Showed Lower Toxicity and Higher Efficacy than Free Drug. The SPR analysis and biodistribution studies revealed that the optimum amount of folate conjugation is of significant importance to achieve passive and active drug targeting simultaneously. From the obtained data above, we selected FMA10 as the optimum micelle composition for further studies, which was believed to be the most suitable for the best performance in terms of tumor-specific drug delivery. In order to elucidate how folate affects in vivo antitumor activity of the micelles in detail, we have injected FMA, MA, and free ADR into the CD-1 nude mice implanted with human pharyngeal cancer KB cells by changing the dosage. Figure 4 show the changes in tumor size and body weight after drug administration. Free ADR was injected as a control, and it suppressed tumor growth at a dose of 10 mg/kg. The mice were also treated with different doses of free ADR, but there was no effect at 5 mg/kg. At a dose of 15 mg/kg, free ADR showed severe toxicity. These results indicated that free ADR was safe to exhibit the efficacy only within an extremely narrow dose range from 10 to 15 mg/kg. Indeed, body weight reduction was observed even at a dose of 10 mg/kg in the case of free ADR. In contrast to free ADR, MA was able to suppress tumor growth over a broad range of doses ranging from 20 to 40 mg/kg, while its toxicity was significantly low. Such effective and safe antitumor activity of the micelles was consistent with our previous results, which demonstrated the usefulness of intracellular pH-sensitive drug delivery (*18, 19*). Nevertheless, the effective dose (ED) of MA was relatively high compared to free ADR. In case of FMA, however, tumor growth was effectively suppressed with the same dose range of MA, but surprisingly, its ED decreased from 20 to 7.5 mg/kg while toxicity remained low. This value is even lower than the ED of free ADR (10 mg/kg), indicating that the micelles became more effective than free drug by folate conjugation. Therefore, these experimental data clearly elucidate that the drug carrier can show higher efficacy than free drug by optimally balancing passive and active tumor targeting properties as well as controlling drug release profile. It should be emphasized that, although the pharmacokinetic study showed that folate conjugation did not significantly improve the tumor-specific accumulation of the micelles, in vivo antitumor activity experiments clearly show that FMA is more effective to the cancer treatment than free ADR in terms of efficacy and safety. These results also support our hypothesis described above that active targeting seems to mainly affect the distribution profile of the drug carriers within the tumor tissues after extravasation rather than in the blood compartment. It is certain that more studies on this topic should be investigated further in the future. Nevertheless, it is of great importance that the ED of FMA decreased compared to free ADR as well as MA. A lowered dose is obviously beneficial for preventing possible long-term toxicity to the patients. From these aspects, it is concluded that our in vivo studies clearly demonstrate the effects of folate conjugation on active targeting drug delivery.

Folate Conjugation Decreased Effective Dose while Maintaining the Broad Therapeutic Window of the Micelles. The range of drug concentrations that provide the efficacy safely is known as the therapeutic window. If the injection dose is lower than this range, the drug cannot show its efficacy. To the contrary, if the injection dose is higher than the therapeutic window, the drug will induce either acute or chronic toxicity. In this study, animal studies have shown that FMA is more effective and safer than free drugs. In order to provide more objective criteria for evaluating efficacy of FMA, we analyzed antitumor activity of the micelles by calculating a treatment to control (T/C) ratio. Figure 5 exhibits the relation between the T/C ratio and a dosage. Each curve provides information about the tumor-suppressing efficacy of FMA, MA, and free ADR

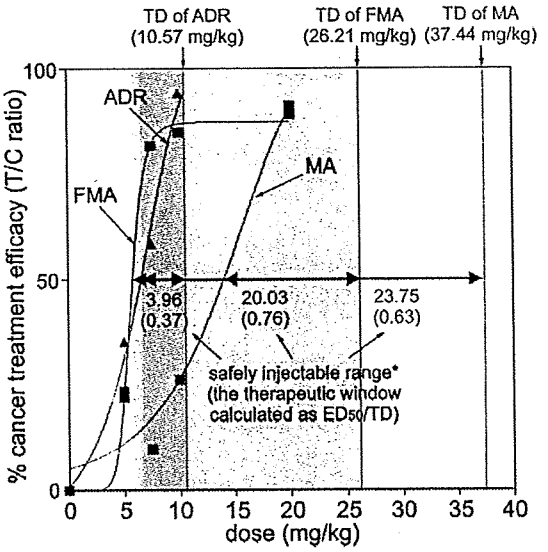

Figure 5. Treatment-to-control (T/C) ratio. Cancer treatment efficacy of the micelles was evaluated by comparing the therapeutic windows of FMA10, MA, and ADR, which were calculated from the ratio of ED_{50} to TD. ED_{50} and TD were defined as the effective dose that induces 50% decrease in tumor volume and the toxic dose that reduces 20% of body weight of mice, respectively. The data show the dose range in which each sample can be safely injected while achieving effective cancer treatments.

with respect to the control. Effective dose (ED) and toxic dose (TD) were defined as the doses that induce 50% of tumor growth (ED_{50}) and reduce 20% of body weight during the treatment, respectively. As drug concentrations increased, tumor growth suppression efficiency increased by all drug formulations. However, when we compare the effective doses, ED_{50} of free ADR is obviously close to its TD while ED_{50} of the micelles remained low compared to their TD. Namely, the safe dose of free ADR was only 3.96 mg/kg, but in contrast, FMA and MA were safely injectable between 20.03 and 23.75 mg/kg, respectively. These values correspond to 5.05- and 5.99-fold broader dose ranges than free drug. In particular, ED_{50} of FMA became lower than that of free ADR, and these results exemplify how active drug targeting is promising for cancer treatment. Most notably, such low toxicity and high efficacy were achieved by determining the optimum amount of folate on the micelle surface.

CONCLUSIONS

Integration of multiple functions into a single nanoparticle can broaden the possibilities of the macromolecular drug delivery systems for their future applications in the clinic. In this study, we have prepared a multifunctional polymeric micelle that is implemented with intracellular pH-dependent drug-releasing functionality and folate-mediated cancer cell targeting property simultaneously. By precision synthesis and preparation of the pH-sensitive micelles with varying folate contents, we were able to elucidate that the ligand-installed micelles for active drug targeting can be more effective than free drug in terms of antitumor activity, safety, pharmacokinetics, and bioavailability. It is of great interest that folate conjugation did not significantly improve the tumor accumulation of the micelles in the body because it induced a prominent increase in accumulation in the liver. However, when folate concentration was adjusted to achieve minimum ligand–receptor interaction, folate-conjugated micelles showed an effective cancer treatment efficiency that was even higher than free drugs as well as the micelles without folate conjugation. These findings clearly demonstrated that the

balance between passive and active drug targeting should be carefully considered to maximize the drug delivery efficiency as well as cytotoxic activity of the polymeric drug carriers.

ACKNOWLEDGMENT

The authors wish to express their thanks for the Project on the Materials Development for Innovative Nano-Drug Delivery Systems from the Ministry of Education, Culture, Sports, Science and Technology (MEXT), Japan.

LITERATURE CITED

(1) Duncan, R. (2006) Polymer conjugates as anticancer nanomedicines. *Nat. Rev. Cancer 6*, 688−701.

(2) Low, P. S., and Antony, A. C. (2004) Folate receptor-targeted drugs for cancer and inflammatory diseases. *Adv. Drug Delivery Rev. 56*, 1055−1058.

(3) Allen, T. M. (2002) Ligand-targeted therapeutics in anticancer therapy. *Nat. Rev. Drug Discovery 2*, 750−763.

(4) Lee, E. S., Na, K., and Bae, Y. H. (2005) Doxorubicin loaded pH-sensitive polymeric micelles for reversal of resistant MCF-7 tumor. *J. Controlled Release 103*, 405−418.

(5) Xu, Z., Gu, W., Huang, J., Sui, H., Zhou, Z., Yang, Y., Yan, Z., and Li, Y. (2005) In vitro and in vivo evaluation of actively targetable nanoparticle for paclitaxel delivery. *Int. J. Pharm. 288*, 361−368.

(6) Oyewumia, M. O., Yokela, R. A., Jaya, M., Coakleyb, T., and Mumper, R. J. (2004) Comparison of cell uptake, biodistribution, and tumor retention of folate-coated and PEG-coated gadolinium nanoparticles in tumor-bearing mice. *J. Controlled Release 95*, 613−626.

(7) Gabizon, A., Horowitz, A. T., Goren, D., Tzemach, D., Shmeeda, H., and Zalipsky, S. (2003) In vivo fate of folate-targeted polyethylene-glycol liposomes in tumor-bearing mice. *Clin. Cancer Res. 9*, 6551−6559.

(8) Jain, R. K. (1998) Delivery of molecular and cellular medicine to solid tumors. *J. Controlled Release 53*, 49−67.

(9) Matsumura, Y., and Maeda, H. (1986) A new concept for macromolecular therapeutics in cancer chemotherapy: mechanism of tumoritropic accumulation of proteins and the antitumor agent Smancs. *Cancer Res. 46*, 6387−6392.

(10) Maeda, H. (2001) SMANCS and polymer-conjugated macromolecular drugs advantages in cancer chemotherapy. *Adv. Drug Delivery Rev. 46*, 169−185.

(11) Minchinton, A. I., and Tannock, I. F. (2006) Drug penetration in solid tumours. *Nat. Rev. Cancer 6*, 583−592.

(12) Kamb, A. (2005) What's wrong with our cancer models? *Nat. Rev. Drug Discovery 4*, 161−165.

(13) Atkins, J. H., and Gershell, L. J. (2002) Selective anticancer drugs. *Nat. Rev. Cancer 1*, 645−646.

(14) Kataoka, K., Harada, A., and Nagasaki, Y. (2001) Block copolymer micelles for drug delivery: design, characterization and biological significance. *Adv. Drug Delivery Rev. 47*, 113−131.

(15) Nishiyama, N., and Kataoka, K. (2006) Nanostructured devices based on block copolymer assemblies for drug delivery: designing structures for enhanced drug function. *Adv. Polym. Sci. 193*, 67−101.

(16) Nishiyama, N., Bae, Y., Miyata, K., Fukushima, S., and Kataoka, K. (2005) Smart polymeric micelles for gene and drug delivery. *Drug Discovery Today: Technol. 2*, 21−26.

(17) Lavasanifar, A., Samuel, J., and Kwon, G. S. (2002) Poly(ethylene oxide)-block poly(L-amino acid) micelles for drug delivery. *Adv. Drug Delivery Rev. 54*, 169−190.

(18) Bae, Y., Fukushima, S., Harada, A., and Kataoka, K. (2003) Design of environment-sensitive supramolecular assemblies for intracellular drug delivery: polymeric micelles that are responsive to intracellular pH change. *Angew. Chem., Int. Ed. 42*, 4640−4643.

(19) Bae, Y., Nishiyama, N., Fukushima, S., Koyama, H., Matsumura, Y., and Kataoka, K. (2005) Preparation and biological characterization of polymeric micelle drug carriers with intracellular pH-triggered drug release property: tumor permeability, controlled subcellular drug distribution, and enhanced in vivo antitumor efficacy. *Bioconjugate Chem. 16*, 122−130.

(20) Mantovani, L. T., Miotti, S., Menard, S., Canevari, S., Raspagliesi, F., Bottini, C., Bottero, F., and Colnaghi, M. I. (1994) Folate binding protein distribution in normal tissues and biological fluids from ovarian carcinoma patients as detected by the monoclonal antibodies MOv18 and MOv19. *Eur. J. Cancer 30A*, 363−369.

(21) Weitman, S. D., Lark, R. H., Coney, L. R., Fort, D. W., Frasca, V., Zurawski, V. R., Jr., and Kamen, B. A. (1992) Distribution of the folate receptor GP38 in normal and malignant cell lines and tissues. *Cancer Res. 52*, 3396−3401.

(22) Hooijberg, J. H., de Vries, N. A., Kaspers, G. J. L., Pieters, R., Jansen, G., and Peters, G. J. (2005) Multidrug resistance proteins and folate supplementation: therapeutic implications for antifolates and other classes of drugs in cancer treatment. *Cancer Chemother. Pharmacol. 58*, 1−12.

(23) Leamon, C. P., and Reddy, J. A. (2004) Folate-targeted chemotherapy. *Adv. Drug Delivery Rev. 56*, 1127−1141.

(24) Lee, R. J., and Low, P. S. (1994) Delivery of liposomes into cultured KB cells via folate receptor-mediated endocytosis. *J. Biol. Chem. 269*, 3198−3204.

(25) Bae, Y., Jang, W.-D., Nishiyama, N., Fukushima, S., and Kataoka, K. (2005) Multifunctional polymeric micelles with folate-mediated cancer cell targeting and pH-triggered drug releasing properties for active intracellular drug delivery. *Mol. BioSyst. 1*, 242−250.

(26) Akiyama, Y., Nagasaki, Y., and Kataoka, K. (2004) Synthesis of heterotelechelic poly(ethylene glycol) derivatives having α-benzaldehyde and ω-pyridyl disulfide groups by ring opening polymerization of ethylene oxide using 4-(diethoxymethyl)benzyl alkoxide as a novel initiator. *Bioconjugate Chem. 15*, 424−427.

(27) Luo, J., Smith, M. D., Lantrip, D. A., Wang, S., and Fuchs, P. L. (1997) Efficient synthesis of pyrofolic acid and pteroyl A azide, reagents for the production of carboxyl differentiated derivatives of folic acid. *J. Am. Chem. Soc. 119*, 10004−10013.

(28) Crouch, S. P., Kozlowski, R., Slater, K. J., and Fletcher, J. (1993) The use of ATP bioluminescence as a measure of cell proliferation and cytotoxicity. *J. Immunol. Methods 160*, 81−88.

(29) Kanie, K., Nishii, M., Yasuda, T., Taki, T., Ujiieb, S., and Kato, T. (2001) Self-assembly of thermotropic liquid-crystalline folic acid derivatives: hydrogen-bonded complexes forming layers and columns. *J. Mater. Chem. 11*, 2875−2886.

(30) Shinoda, T., Takagi, A., Maeda, A., Kagatani, S., Konno, Y., and Hashida, M. (1998) In vivo fate of folate-BSA in non-tumor- and tumor-bearing mice. *J. Pharm. Sci. 87*, 1521−1526.

BC060401P

Langmuir **2007**, *23*, 6698−6703

Density Control of Poly(ethylene glycol) Layer To Regulate Cellular Attachment

Tomomi Satomi,[†,‡,§,||] Yukio Nagasaki,[⊥] Hisatoshi Kobayashi,[§] Hidenori Otsuka,[*,†,‡,§] and Kazunori Kataoka[||,#]

Department of Applied Chemistry, Faculty of Science, Tokyo University of Science, 1-3 Kagurazaka, Shinjuku-ku, Tokyo 162-8601, Japan, Division of Bioengineering and Bioinformatics, Graduate School of Information Science and Technology, Hokkaido University, North 14 West 9, Sapporo 060-0814, Japan, Biomaterials Center, National Institute for Materials Science (NIMS), 1-1 Namiki, Tsukuba, Ibaraki 305-0044, Japan, Division of Clinical Biotechnology, Center for Disease Biology and Integrative Medicine, Graduate School of Medicine, The University of Tokyo, 7-3-1 Hongo, Bunkyo-ku, Tokyo 113-0033, Japan, Graduate School of Pure and Applied Sciences, University of Tsukuba, 1-1-1 Tenodai, Tsukuba, Ibaraki 305-8571, Japan, and Department of Materials Science and Engineering, Graduate School of Engineering, The University of Tokyo, 7-3-1 Hongo, Tokyo 113-8656, Japan

Received August 17, 2006. In Final Form: March 7, 2007

A wide variety of cells usually integrate and respond to the microscale environment, such as soluble protein factors, extracellular matrix proteins, and contacts with neighboring cells. To gain insight into cellular microenvironment design, we investigated two-dimensional microarray formation of endothelial cells on a micropatterned poly(ethylene glycol) (PEG)-brushed surface, based on the relationship between PEG chain density and cellular attachment. The patterned substrates consisted of two regions: the PEG surface that acts as a cell-resistant layer and the exposed substrate surface that promotes protein or cell adsorption. A PEG-brushed layer was constructed on a gold substrate using PEG with a mercapto group at the end of the chain. The density of the PEG-brushed layer increased substantially with repetitive adsorption/rinse cycles of PEG on the gold substrate, allowing marked reduction of nonspecific protein adsorption. These repeated adsorption/rinse cycles were further regulated by using longer (5 kDa) and shorter (2 kDa) PEG to construct PEG layers with different chain density, and subsequent micropatterning was achieved by plasma etching through a micropatterned metal mask. The effects of PEG chain density on pattern formation of cell attachment were determined on micropatterning of endothelial cells. The results indicated that cell pattern formation was strongly dependent on the PEG chain density and on the extent of protein adsorption. Notably, a PEG chain density high enough to inhibit outgrowth of endothelial cells from the cell-adhering region in the horizontal direction could be obtained only by employing formation of a short filler layer of PEG in the preconstructed longer PEG-brushed layer, which prevented nonspecific protein adsorption almost completely. In this way, a completely micropatterned array of endothelial cells with long-term viability was obtained. This clearly indicated the importance of a short underbrushed PEG layer in minimizing nonspecific protein adsorption for long-term maintenance of the active cell pattern. The strategy for cell patterning presented here can be employed in tissue engineering to study cell−cell and cell−surface interactions. It is also applicable for high-throughput screening and clinical diagnostics, as well as interfacing cellular and microfabricated components of biomedical microsystems.

Introduction

Surface engineering techniques for cellular micropatterning are emerging as important tools to clarify the effects of the microenvironment on cellular behavior,[1,2] as cells usually integrate and respond to the microscale environment, such as chemical and mechanical properties of the surrounding fluid and extracellular matrix, soluble protein factors, small signal molecules, and contacts with neighboring cells.[3,4] Furthermore, living cells undergo physiological changes in response to exposure to drugs and environmental perturbations, such as toxins, pathogens, or other agents, and thus high-throughput technologies using whole cells have also been developed.[5−13] To develop this kind of cellular microarray composed of a cell-resistant surface and cell attachment region, micropatterning a protein-repellent surface is important because cellular adhesion and proliferation are regulated by protein adsorption.

* Corresponding author. Address: Hidenori Otsuka, Ph.D., Department of Applied Chemistry, Faculty of Science, Tokyo University of Science, 1-3 Kagurazaka, Shinjuku-ku, Tokyo 162-8601, Japan. Phone: +81-3-5228-8265. Fax: +81-3-5228-8265. E-mail: h.otsuka@rs.kagu.tus.ac.jp.

† Tokyo University of Science.

‡ Hokkaido University.

§ National Institute for Materials Science.

|| Graduate School of Medicine, The University of Tokyo.

⊥ University of Tsukuba.

Graduate School of Engineering, The University of Tokyo.

(1) Whitesides, G. M.; Ostuni, E.; Takayama, S.; Jiang, X.; Ingber, D. E. *Annu. Rev. Biomed. Eng.* **2001**, *3*, 335.

(2) Jeon, N. L.; Baskaran, H.; Detringer, S. K. W.; Whitesides, G. M.; Van de Water, L.; Toner, M. *Nat. Biotechnol.* **2002**, *20*, 826.

(3) Zamir, E.; Katz, B. Z.; Aota, K. M.; Yamada, K. M.; Geiger, B.; Kam, Z. *J. Cell Sci.* **1999**, *112*, 1655.

(4) Geiger, B.; Bershadsky, R.; Pankov, R.; Yamada, K. M. *Nat. Rev. Mol. Cell Biol.* **2001**, *2*, 793.

(5) Stenger, D. A.; Gross, G. W.; Keefer, E. W.; Shaffer, K. M.; Andreadis, J. D.; Ma, W.; Pancrazio, J. J. *Trends Biotechnol.* **2001**, *19*, 304.

(6) Kononen, J.; Bubendorf, L.; Kallioniemi, A.; Barlund, M.; Schraml, P.; Leighton, S.; Torhorst, J.; Mihatsch, M. J.; Sauter, G.; Kallioniemi, O. P. *Nat. Med.* **1998**, *4*, 844.

(7) Ziauddin, J.; Sabatini, D. M. *Nature* **2001**, *411*, 107.

(8) Michalopoulos, G. K.; DeFrances, M. C. *Science* **1997**, *276*, 60.

(9) Anderson, D. G.; Levenberg, S.; Langer, R. *Nat. Biotechnol.* **2004**, *22*, 863.

(10) Revzin, A.; Tompkins, R. G.; Toner, M. *Langmuir* **2003**, *19*, 9855.

(11) Thielecke, H.; Mack, A.; Robitzki, A. *Biosens. Bioelectron.* **2001**, *16*, 261.

(12) Mack, A. R.; Thielecke, H.; Robitzki, A. A. *Trends Biotechnol.* **2002**, *20*, 56.

(13) Otsuka, H.; Hirano, A.; Nagasaki, Y.; Okano, T.; Horiike, Y.; Kataoka, K. *ChemBioChem* **2004**, *5*, 850.

10.1021/la0624384 CCC: $37.00
Published on Web 05/05/2007

balance between passive and active drug targeting should be carefully considered to maximize the drug delivery efficiency as well as cytotoxic activity of the polymeric drug carriers.

ACKNOWLEDGMENT

The authors wish to express their thanks for the Project on the Materials Development for Innovative Nano-Drug Delivery Systems from the Ministry of Education, Culture, Sports, Science and Technology (MEXT), Japan.

LITERATURE CITED

(1) Duncan, R. (2006) Polymer conjugates as anticancer nanomedicines. *Nat. Rev. Cancer 6*, 688−701.

(2) Low, P. S., and Antony, A. C. (2004) Folate receptor-targeted drugs for cancer and inflammatory diseases. *Adv. Drug Delivery Rev. 56*, 1055−1058.

(3) Allen, T. M. (2002) Ligand-targeted therapeutics in anticancer therapy. *Nat. Rev. Drug Discovery 2*, 750−763.

(4) Lee, E. S., Na, K., and Bae, Y. H. (2005) Doxorubicin loaded pH-sensitive polymeric micelles for reversal of resistant MCF-7 tumor. *J. Controlled Release 103*, 405−418.

(5) Xu, Z., Gu, W., Huang, J., Sui, H., Zhou, Z., Yang, Y., Yan, Z., and Li, Y. (2005) In vitro and in vivo evaluation of actively targetable nanoparticle for paclitaxel delivery. *Int. J. Pharm. 288*, 361−368.

(6) Oyewumia, M. O., Yokela, R. A., Jaya, M., Coakleyb, T., and Mumper, R. J. (2004) Comparison of cell uptake, biodistribution, and tumor retention of folate-coated and PEG-coated gadolinium nanoparticles in tumor-bearing mice. *J. Controlled Release 95*, 613−626.

(7) Gabizon, A., Horowitz, A. T., Goren, D., Tzemach, D., Shmeeda, H., and Zalipsky, S. (2003) In vivo fate of folate-targeted polyethyleneglycol liposomes in tumor-bearing mice. *Clin. Cancer Res. 9*, 6551−6559.

(8) Jain, R. K. (1998) Delivery of molecular and cellular medicine to solid tumors. *J. Controlled Release 53*, 49−67.

(9) Matsumura, Y., and Maeda, H. (1986) A new concept for macromolecular therapeutics in cancer chemotherapy: mechanism of tumoritropic accumulation of proteins and the antitumor agent Smancs. *Cancer Res. 46*, 6387−6392.

(10) Maeda, H. (2001) SMANCS and polymer-conjugated macromolecular drugs advantages in cancer chemotherapy. *Adv. Drug Delivery Rev. 46*, 169−185.

(11) Minchinton, A. I., and Tannock, I. F. (2006) Drug penetration in solid tumours. *Nat. Rev. Cancer 6*, 583−592.

(12) Kamb, A. (2005) What's wrong with our cancer models? *Nat. Rev. Drug Discovery 4*, 161−165.

(13) Atkins, J. H., and Gershell, L. J. (2002) Selective anticancer drugs. *Nat. Rev. Cancer 1*, 645−646.

(14) Kataoka, K., Harada, A., and Nagasaki, Y. (2001) Block copolymer micelles for drug delivery: design, characterization and biological significance. *Adv. Drug Delivery Rev. 47*, 113−131.

(15) Nishiyama, N., and Kataoka, K. (2006) Nanostructured devices based on block copolymer assemblies for drug delivery: designing structures for enhanced drug function. *Adv. Polym. Sci. 193*, 67−101.

(16) Nishiyama, N., Bae, Y., Miyata, K., Fukushima, S., and Kataoka, K. (2005) Smart polymeric micelles for gene and drug delivery. *Drug Discovery Today: Technol. 2*, 21−26.

(17) Lavasanifar, A., Samuel, J., and Kwon, G. S. (2002) Poly(ethylene oxide)-block poly(L-amino acid) micelles for drug delivery. *Adv. Drug Delivery Rev. 54*, 169−190.

(18) Bae, Y., Fukushima, S., Harada, A., and Kataoka, K. (2003) Design of environment-sensitive supramolecular assemblies for intracellular drug delivery: polymeric micelles that are responsive to intracellular pH change. *Angew. Chem., Int. Ed. 42*, 4640−4643.

(19) Bae, Y., Nishiyama, N., Fukushima, S., Koyama, H., Matsumura, Y., and Kataoka, K. (2005) Preparation and biological characterization of polymeric micelle drug carriers with intracellular pH-triggered drug release property: tumor permeability, controlled subcellular drug distribution, and enhanced in vivo antitumor efficacy. *Bioconjugate Chem. 16*, 122−130.

(20) Mantovani, L. T., Miotti, S., Menard, S., Canevari, S., Raspagliesi, F., Bottini, C., Bottero, F., and Colnaghi, M. I. (1994) Folate binding protein distribution in normal tissues and biological fluids from ovarian carcinoma patients as detected by the monoclonal antibodies MOv18 and MOv19. *Eur. J. Cancer 30A*, 363−369.

(21) Weitman, S. D., Lark, R. H., Coney, L. R., Fort, D. W., Frasca, V., Zurawski, V. R., Jr., and Kamen, B. A. (1992) Distribution of the folate receptor GP38 in normal and malignant cell lines and tissues. *Cancer Res. 52*, 3396−3401.

(22) Hooijberg, J. H., de Vries, N. A., Kaspers, G. J. L., Pieters, R., Jansen, G., and Peters, G. J. (2005) Multidrug resistance proteins and folate supplementation: therapeutic implications for antifolates and other classes of drugs in cancer treatment. *Cancer Chemother. Pharmacol. 58*, 1−12.

(23) Leamon, C. P., and Reddy, J. A. (2004) Folate-targeted chemotherapy. *Adv. Drug Delivery Rev. 56*, 1127−1141.

(24) Lee, R. J., and Low, P. S. (1994) Delivery of liposomes into cultured KB cells via folate receptor-mediated endocytosis. *J. Biol. Chem. 269*, 3198−3204.

(25) Bae, Y., Jang, W.-D., Nishiyama, N., Fukushima, S., and Kataoka, K. (2005) Multifunctional polymeric micelles with folate-mediated cancer cell targeting and pH-triggered drug releasing properties for active intracellular drug delivery. *Mol. BioSyst. 1*, 242−250.

(26) Akiyama, Y., Nagasaki, Y., and Kataoka, K. (2004) Synthesis of heterotelechelic poly(ethylene glycol) derivatives having α-benzaldehyde and ω-pyridyl disulfide groups by ring opening polymerization of ethylene oxide using 4-(diethoxymethyl)benzyl alkoxide as a novel initiator. *Bioconjugate Chem. 15*, 424−427.

(27) Luo, J., Smith, M. D., Lantrip, D. A., Wang, S., and Fuchs, P. L. (1997) Efficient synthesis of pyrofolic acid and pteroyl A azide, reagents for the production of carboxyl differentiated derivatives of folic acid. *J. Am. Chem. Soc. 119*, 10004−10013.

(28) Crouch, S. P., Kozlowski, R., Slater, K. J., and Fletcher, J. (1993) The use of ATP bioluminescence as a measure of cell proliferation and cytotoxicity. *J. Immunol. Methods 160*, 81−88.

(29) Kanie, K., Nishii, M., Yasuda, T., Taki, T., Ujiieb, S., and Kato, T. (2001) Self-assembly of thermotropic liquid-crystalline folic acid derivatives: hydrogen-bonded complexes forming layers and columns. *J. Mater. Chem. 11*, 2875−2886.

(30) Shinoda, T., Takagi, A., Maeda, A., Kagatani, S., Konno, Y., and Hashida, M. (1998) In vivo fate of folate-BSA in non-tumor- and tumor-bearing mice. *J. Pharm. Sci. 87*, 1521−1526.

BC060401P

A number of approaches to construct protein-repellent and subsequent cell-repellent surfaces have been studied using polymer coating. In fact, there has been a great deal of discussion regarding the molecular properties on the surface, and it is widely believed that effective protein rejection requires the bound polymer to be heavily hydrated, densely packed, neutral, deposited in a thick layer, and conformationally mobile.[14−18] Here, we focus on poly(ethylene glycol) (PEG), one of the most useful polymers to repel protein. Surface modification by PEG leads to a significant reduction in the nonspecific interaction of biological molecules with the surface due to its high degree of hydrophilicity and chain flexibility, inducing an effective exclusion volume effect.[19−22] Most previous studies of surfaces with immobilized PEG have described higher protein-repellent ability with longer chain, resulting in increasing thickness of PEG,[23−27] which is considered to be due to the stronger attenuation of the long-range Lifshitz−van der Waals attraction. However, immobilization of longer PEG chains results in a decrease in chain density due to its larger exclusion volume effect, although it has a sufficiently large separation between the surface and proteins. Conversely, immobilization of shorter PEG chains gives higher density due to its smaller exclusion volume effect, although it has a smaller separation between the surface and proteins. To resolve this controversial issue of the length and density of the PEG layer, we previously reported the development of surface construction using long and short PEG chains; formation of a short, filler layer of PEG in the preconstructed longer PEG-brushed layer prevented nonspecific protein adsorption almost completely.[28] In most studies of this type, a protein-repellent surface will be expected to repel cellular attachment. However, the question of how dense the immobilized PEG chain must be to control cell attachment has still not been answered.

The present study was performed to determine the influence of PEG chain density on cellular attachment directly. For the micropatterning of cells, it is necessary to prevent overgrowth of cells from the cell-adhering pattern; i.e., construction of a cytophobic surface is important for micropatterning. Here, we controlled the modification ratio of long and short PEG chains to construct surfaces with different PEG chain densities, and subsequent micropatterning was achieved by plasma etching through a micropatterned metal mask ($\phi = 100\ \mu$m, edge-to-edge spacing of $l = 300\ \mu$m). The relationship between PEG chain density and cellular attachment is discussed on micropatterning of endothelial cells.

Experimental Section

Materials. Poly(ethylene glycol) (PEG) with a methoxy group at one end and a mercapto group at the other (MeO−PEG−SH) was provided by NOF Corporation (Tokyo, Japan). The molecular weight and polydispersity of PEGs, denoted by PEG2k and PEG5k, were 2096 and 1.05 and 5341 and 1.04, respectively. Gold chips (SIA KIT Au) for SPR measurements were purchased from Biacore AB (Uppsala, Sweden). Human umbilical endothelial cells (HUVEC) were purchased from Cambrex (Cambrex BioScience Walkersville, Inc., Walkersville, MD). HUVECs were cultured in EBM-2 medium (Cambrex). Water used in this study was purified by passing it through a Milli-Q System (Nihon Millipore Co., Tokyo, Japan) until its specific conductivity fell below 0.1 μS cm^{-1}.

1. PEG Immobilization Study. *Preparation of MeO−PEG−SH-Modified Gold Surface.* Immobilization of PEG on the gold sensor chip surface was performed using a surface plasmon resonance (SPR) instrument (Biacore X; Biacore AB, Uppsala, Sweden). Phosphate buffered saline (PBS; pH 7.4, 0.15 M, containing 1 M NaCl) solutions of PEG were injected at a flow rate of 10 μL/min for 10 min at 37 °C under running PBS (pH 7.4, 0.15 M, containing 1 M NaCl). An SPR sensorgram on the gold sensor chip for this adsorption/rinsing (with running PBS) of PEG was monitored, and the amount of immobilized PEG was assessed by the SPR angle shift. PEG solutions with different concentrations were injected on a sensor chip, and then the plateau region for PEG immobilization was determined. To increase (or change) the amount of immobilized PEG, the process of PEG injection was repeated several times according to the reported method.[24] PEGylated surfaces prepared by one, two, and three repetitive injections were denoted as PEG5k(1), PEG5k(2), and PEG5k(3) surfaces, respectively. In a manner similar to the above-repeated process, successive PEGylation with longer and then shorter PEG was carried out. A shorter PEG (PEG2k) as a filler was layered on the surface with the preconstructed longer PEG brushes (PEG5k) by repetitive injection. PEG5k(1) surfaces with three treatments with the filler PEG and PEG5k(2) with four treatments with the filler PEG were denoted as PEG5k(1)/2k(3) and PEG5k(2)/2k(4) surfaces, respectively.

The density of immobilized PEG chains was estimated quantitatively by quartz crystal microbalance (QCM) measurement using an AT-cut gold-sputtered quartz crystal with a resonance frequency of 27 MHz (Initium Inc., Japan). The frequency was recorded after immersing the crystals in the PBS (pH 7.4, 0.15 M, containing 1 M NaCl) at 37 °C. After baseline stabilization, PEG solutions (PEG5k, PEG2k) were injected at a concentration of 0.01 mg/mL, which was optimized above in the same repetitive manner as in SPR measurement (PEG5k(3), PEG5k(1)/2k(3), PEG5k(2)/2k(4)).

Surface Characterization. The wettability of all PEGylated surfaces was estimated from the static and dynamic contact angle measurements (CA-W contact angle meter; Kyowa Interface Science Co., Ltd., Tokyo, Japan).[29] Gold and PEGylated gold surfaces were constructed on glass substrates as described in detail in the section describing the cell culture study (see "Construction of PEGylated surface"). Water-in-air and air-in-water systems were applied in the static contact angle measurements. Water-in-air system measurement was performed by a sessile droplet technique, where a water droplet (Milli-Q quality) was placed on the sample surface at 25 °C. The air-in-water system procedure followed the captive bubble technique, where the sample surface was immersed in water maintained at 25 °C and a small air bubble was placed on the sample surface from the bottom using a curved needle. The contact angle of each surface was measured on 10 spots, and the obtained values were averaged.

For dynamic contact angle measurements, the advancing (θ_{adv}) and receding (θ_{rec}) contact angles were obtained by extending and then contracting the volume (5.9 μL) of the water droplet using a motor-driven syringe at a rate of 1.88 μL/s for 3.1 s. The extending/contracting droplet was monitored with a CCD camera; each picture was captured every 67 ms, and 24 images were taken for both θ_{adv} and θ_{rec}, when the water droplet volume was changed at 1.88 μL/s. The contact angles were evaluated from video printouts of the droplet.

(14) Lee, J. H.; Kopeckova, P.; Kopecek, J.; Andrade, J. D. *Biomaterials* **1990**, *11*, 455.
(15) Desai, N. P.; Hubbell, J. A. *Macromolecules* **1992**, *25*, 226.
(16) Bergstrom, K.; Osterberg, E.; Holmberg, K.; Riggs, J. A.; Van Alstime, J. M.; Schuman, T. P.; Burns, N. L.; Harris, J. M. *Colloids Surf. A* **1993**, *77*, 159.
(17) Sofia, S. J.; Premnath, V.; Merrill, E. W. *Macromolecules* **1998**, *31*, 5059.
(18) Osterberg, E.; Bergstrom, K.; Holmberg, K.; Schuman, T. P.; Riggs, J. A.;. Burns, N. L; Van Alstine, J. M.; Harris, J. M. *J. Biomed. Mater. Res.* **1995**, *29*, 741.
(19) Mori, Y.; Nagaoka, S.; Takiuchi, H.; Kikuchi, T.; Noguchi, N.; Tanzawa, H.; Noishiki, Y. *Trans. Am. Soc. Artif. Internal Organs* **1982**, *28*, 459.
(20) Bergstrom, K.; Osterberg, E.; Holmberg, K.; Hoffman, A. S.; Schuman, T. P.; Kozlowski, A.; Harris, J. M. *J. Biomater. Sci. Polym. Ed.* **1994**, *6*, 123.
(21) Harris, J. M., Ed. *Poly(ethylene glycol) Chemistry, Biotechnical and Biomedical Applications*; Plenum Press: New York, 1992.
(22) Glass, J. E., Ed. *Hydrophilic Polymers, Performance with Environmental Acceptance*; American Chemical Society: Washington DC, 1996.
(23) Prime, K. L.; Whiteside, G. M. *J. Am. Chem. Soc.* **1993**, *115*, 10714.
(24) Gombotz, W. R.; Guanghui, W.; Horbett, T. A.; Hoffman, A. S. *J. Biomed. Mater. Res.* **1991**, *25*, 1547.
(25) Lee, J.; Martic, P. A.; Tan, J. S. *J. Colloid Interface Sci.* **1989**, *131*, 252.
(26) Jeon, S. I.; Andrade, J. D.; de Gennes, P. G. *J. Colloid Interface Sci.* **1991**, *142*, 159.
(27) Roosjen, A.; van der Mei, H. C.; Busscher, H. J.; Norde, W. *Langmuir* **2004**, *20*, 10949.
(28) Uchida, K.; Otsuka, H.; Kaneko, M.; Kataoka, K.; Nagasaki, Y. *Anal. Chem.* **2005**, *77*, 1075.
(29) Otsuka, H.; Nagasaki, Y.; Kataoka, K. *Biomacromolecules* **2000**, *1*, 39.

Protein Adsorption Study. A protein adsorption study, which is an important reference for cell attachment, was performed using SPR equipment. Before the protein adsorption study, three types of PEGylated surface were constructed on a gold sensor chip in the same manner as described above: PEG5k(3), PEG5k(1)/2k(3), and PEG5k(2)/2k(4). And then protein adsorption was estimated by flowing 100 μL of serum-containing medium (EBM-2 medium to culture HUVEC) at a flow rate of 10 μL/min at 37 °C under running PBS (pH 7.4, 0.15 M) on the three types of PEGylated surface and native gold surface. The magnitude of the SPR angle shift by this injection was measured from the data taken from the final part of the curve after the surfaces were rinsed, and assessed as the amount of protein adsorbed. As a control, protein adsorption on a bare gold surface was examined.

2. Cell Culture Study. *Construction of PEGylated Surface.* Glass slides were etched with a boiling mixture of 50% (v/v) sulfuric acid and 50% (v/v) hydrogen peroxide for 30 min and then rinsed thoroughly with water. At 10^{-6} Torr, a 10 Å film of chromium was vapor-deposited at a rate of 0.1 Å/s onto the glass substrate. A 200 Å film of gold was then vapor-deposited on top of it at a rate of 0.1 Å/s. PEGylated surfaces were prepared on the gold films in the same manner as described for SPR measurements. PBS (pH 7.4, 0.15 M, containing 1 M NaCl) solutions of PEG5k (0.01 mg/mL) and PEG2k (0.01 mg/mL) were prepared. Then, PEG solutions with the appropriate conditions were retained on the gold film for 30 min to construct the PEGylated surfaces described above (PEG5k(3), PEG5k(1)/2k(3), PEG5k(2)/2k(4)). The plates were washed with Milli-Q water between each PEGylation, for 5 min each time.

Micropatterning of PEGylated Surface. The micropattern on the PEGylated surfaces were obtained by $N_2 + H_2$ plasma etching using a metal mask with holes 100 μm in diameter spaced 300 μm apart. After construction of a 2-well plastic chamber (Falcon BD) on the glass thus prepared, all samples were sterilized with ethylene oxide gas.

Cell Culture Study. HUVECs were seeded onto the micropatterned PEGylated surface at a cell density of 1×10^6 cells/mL. Cells were cultured at 37 °C in a humidified atmosphere of 5% CO_2. An EBM-2 medium was used for cultivation and was exchanged every 2 days.

Results and Discussion

Micropatterned PEGylated substrates with two-dimensional arrays of plasma-etched circular domains (ϕ = 100 μm) were prepared by sequential immobilization of PEG possessing a mercapto group at the end of the chain on the gold substrate, followed by plasma etching through a metal mask pattern with circular holes. The PEGylated region on the patterned substrate acts to repel proteins and thus inhibits cell adhesion. Proteins are expected to adsorb from the serum-containing medium onto the plasma-etched circular domains, exposing the base gold surface.

1. PEG Immobilization Study. The surface properties of the PEG coating were studied in detail to estimate protein adsorption and subsequent cell culture study on PEGylated surfaces. First, PBS solutions of various concentrations of PEG including 1 M NaCl were injected onto the gold surface using an SPR instrument to optimize immobilized concentration on a sensor chip. Use of high ionic strength buffer caused an increase in the amount of immobilized PEG, due to the appreciably reduced solubility of PEG in concentrated buffer solution.[30] The changes in SPR angle at each concentration of PEG5k are plotted in Figure 1. The results confirmed that the amount of immobilized PEG increased with increases in the injected PEG concentration; saturation was observed at PEG concentrations over 0.01 mg/mL, suggesting that the amount of possible immobilization on the gold surface is constant with injection of PEG above this concentration. There were no significant differences in this PEG immobilization study between PEG2k and PEG5k. Therefore, immobilization of PEG

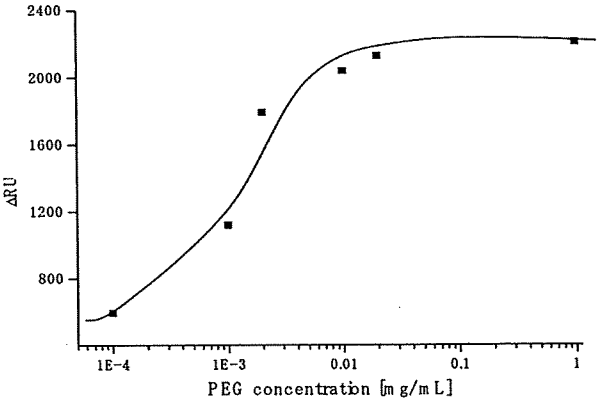

Figure 1. PEG immobilization as a function of PEG concentration. Flow rate, 10 μL/min; running buffer, PBS (pH 7.4, 0.15 M, containing 1 M NaCl); sample, PEG (M_w: 5k)/PBS (0.15 M, pH 7.4, containing 1 M NaCl) solution; sample injection, 100 μL.

on the gold surface was performed with 0.01 mg/mL PEG solution. Three types of PEG immobilization (PEG5k(3), PEG5k(1)/2k-(3), PEG5k(2)/2k(4), as described in the experimental section) were performed at this concentration, as shown in SPR sensorgrams (Figure 2). After first treatment with PEG5k, the sensor surface was washed under running buffer to remove noncovalently adsorbed PEG. The sensor chip was then treated again with a solution of PEG5k. This cycle of adsorption/rinsing of PEG5k was repeated several times. Eventually, the total SPR angle shift was amplified by increasing the number of treatment cycles to three, indicating that repetitive treatment with PEG5k was effective in increasing the density of PEG (PEG5k(3)). Notably, this trend became even more significant following additional treatment of the PEG5k surface with shorter PEG (PEG2k), as shown in Figure 2b,c. We planned to increase the surface brush density by PEG2k, retaining the PEG5k brush surface character. Sensorgrams showed a number of interesting findings. First, immobilization of long-chain PEG (PEG5k(1)) increased markedly with changes in SPR angle (Figure 2a–c). However, the extent of the shift decreased with the second injection of long-chain PEG (PEG5k(2)) (Figure 2a,c), and little change was seen on the third injection of long-chain PEG (PEG5k-(3)) (Figure 2a). On the other hand, immobilization of short-chain PEG (PEG2k(1)) after long-chain PEG resulted again in marked changes (Figure 2b,c). These results suggested that long-chain PEG5k can hardly penetrate into the preconstructed longer PEG-brushed layer due to its exclusion volume effect, while short-chain PEG2k appreciably filled the gap in the preconstructed longer PEG layer. It should be noted that SPR sensorgrams showed a steep increase curve in PEG2k(1), as shown in Figure 2b,c, indicating the importance of a short underbrushed PEG layer in increasing the PEG chain density.

To confirm that these SPR angle changes are reflected directly in the amount of immobilized PEG, QCM measurement was performed in the same manner as SPR (Table 1). The average value of total frequency shift after PEG injection is given as Δf in Table 1. PEG5k(2)/2k(4) surface showed the largest frequency shift, and PEG5k(1)/2k(3) surface also showed around 2000 Hz in frequency shift. On the other hand, PEG5k(3) surface showed around 1400 Hz in total frequency shift. Thus, PEG5k surface mixed with PEG2k showed larger mass change than only PEG5k chain immobilization, which suggested that more PEG chains were immobilized in PEG5k and PEG2k mixed surface. This result also indicated a significant role of a short underbrushed PEG layer in increasing the PEG chain density. On QCM

(30) Emoto, K.; Harris, J. M.; Alstine, M. V. *Anal. Chem.* **1996**, *68*, 3751.

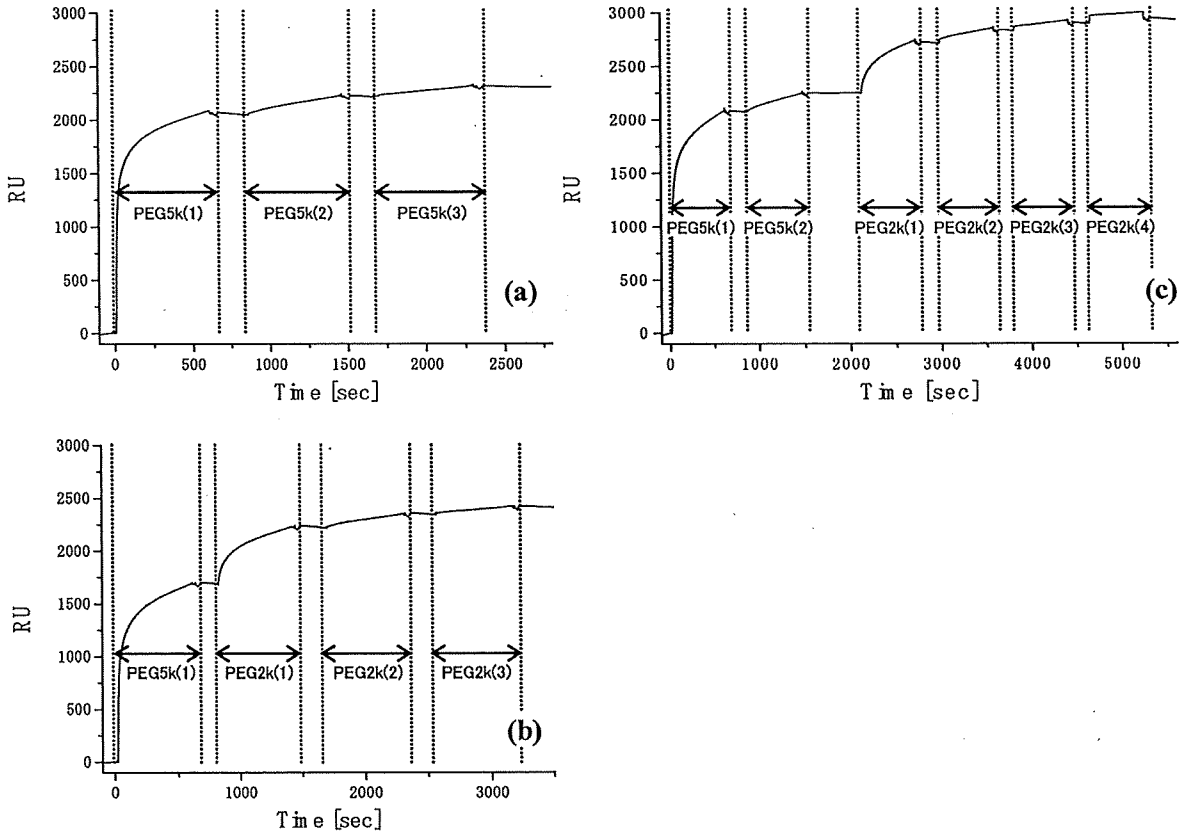

Figure 2. Sensorgrams of PEG immobilization on gold surfaces. (a) PEG5k(3), (b) PEG5k(1)/2k(3), and (c)PEG5k(2)/2k(4). Flow rate, 10 μL/min; running buffer, PBS (0.15 M, pH 7.4, containing 1 M NaCl); sample, 0.01 mg/mL of PEG (M_w: 5k or 2k)/PBS (0.15 M, pH7.4, containing 1 M NaCl) solution; sample injection, 100 μL for each time point.

Table 1. Comparison of Three Types of PEG Immobilization Measured by QCM: Δf is the Average of Total Frequency Shift after PEG Immobilization (n = 3)

PEG surfaces	Δf (Hz)	±S.D.
5k(3)	1382.8	118.6
5k(1)/2k(3)	1922.8	92.70
5k(2)/2k(4)	2144.7	81.74

measurement, the PEG5k(2)/2k(4) surface was determined to have the highest PEG chain density, while PEG5k(3) had the lowest.

The static wettability of the surface coated with PEG was estimated in both air and water by contact angle measurement (Figure 3). In the water-in-air measurement, the coating of PEG on the gold substrate significantly increased its wettability, as indicated by a decrease in the static contact angle (~30°). A similar trend was observed in the air-in-water measurement and the effect of PEG density on wettability was more pronounced, showing progressively increasing contact angle with increasing PEG chain density. Note that the increase in contact angle corresponds to an increase in wettability for the air-in-water system. As the accuracy of contact angle is ±2°, as shown by Zisman and co-worker,[31] significant differences could be seen between PEG surfaces. Furthermore, advancing/receding contact angles and hysteresis were measured on each PEG surface to estimate the dynamics of the uppermost surface in detail (Figure 4). In receding contact angles, each PEG surface showed a small value of around 15−20° and there was little difference between surfaces. On the other hand, critical differences were observed

(31) Fox, H. W.; Zisman, W. A. *J. Colloid Sci.* **1950**, *5*, 514.

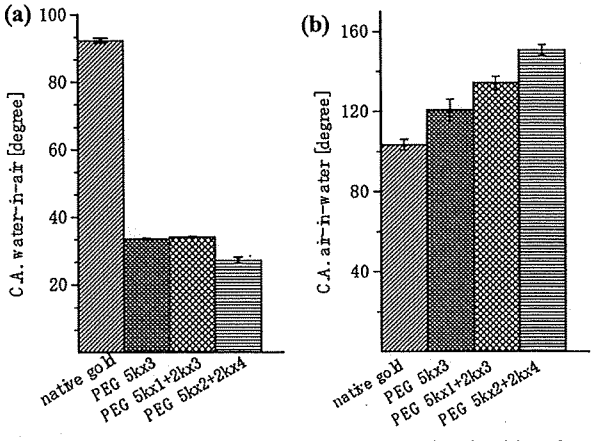

Figure 3. Static water contact angles on PEGylated gold surface. (a) Water-in-air system; (b) air-in-water system.

in advancing contact angles. PEG5k(3) and PEG5k(1)/2k(3) surfaces had around 30°, while the value for the PEG5k(2)/2k(4) surface was almost half. As PEG surfaces are easy to hydrate and show good water retentivity, once they became wet, receding contact angles showed small values in all PEG surfaces, resulting in little difference in receding contact angle. In contrast, significant differences were observed in advancing contact angles, indicating that the PEG5k(2)/2k(4) surface has the greatest wettability in the dry to wet state as compared with the other PEG surfaces examined. Hysteresis indicated differences between PEG5k(2)/2k(4) surfaces and the other surfaces according to its high surface free energy. When the water droplet extends, the surface with

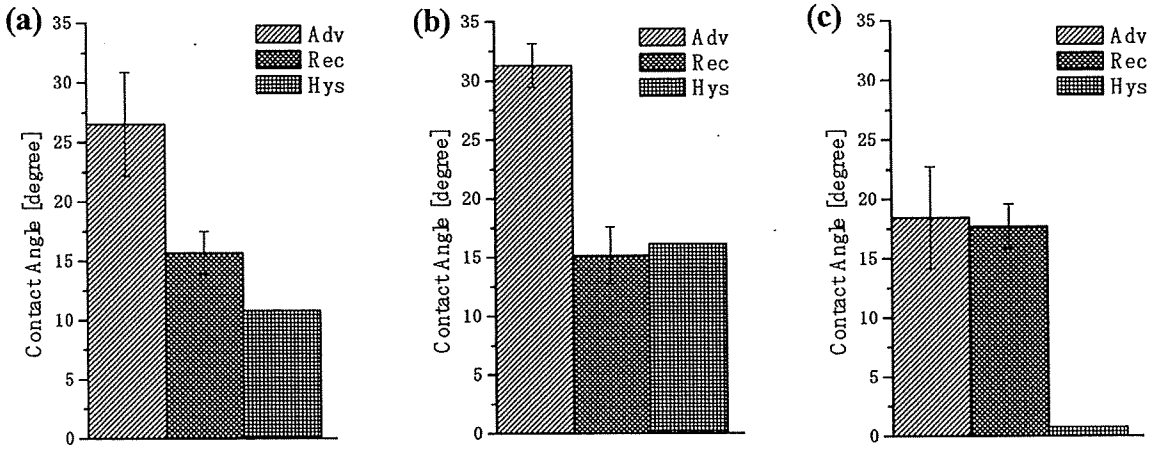

Figure 4. Dynamic water contact angles on PEGylated gold surfaces. (a) PEG5k(3), (b) PEG5k(1)/2k(3), and (c) PEG5k(2)2k(4).

a high surface free energy facilitates penetration of water, aiding in water droplet spreading, while the surface prevents the water droplet from receding when it contracts. Accordingly, the observations of the present study suggested that the PEG5k-(2)/2k(4) surface is the most hydrophilic and has a high surface free energy due to its high PEG chain density. Furthermore, the chain density is reported to have the relation with other parameters including the thickness and conformation of PEG layer.[23−27,32,33] The PEG chains (5k and 2k) are more well-oriented in this surface since the short, filler-like PEG2k chains will enhance the lateral interactions (e.g., hydrogen bonding and van der Waals force) between the PEG chains. This will likely result in much enhanced water affinity/penetration capability in PEG chains during the advancing angle measurement. Therefore, only small hysteresis value will be found on a PEG5k(2)/2k(4) surface.

Nonspecific protein adsorption from the culture medium for HUVEC was estimated on each PEG-coated surface to estimate the cytophobicity of PEGylated surfaces because the adsorbed proteins are responsible for subsequent cell adhesion. On bare gold as a control, the SPR angle shift due to the nonspecific adsorption of protein was 2927.4 RU, when a serum-containing cell (HUVEC) culture medium (EBM-2) was passed over the surface for 10 min at a flow rate of 10 μL/min. In contrast, PEG-coated surfaces clearly reduced protein adsorption (Figure 5). Figure 5 also shows a comparison of protein adsorption on the three types of PEG surface. The SPR angle shift was 676.5, 350.8, and 218.0 RU on PEG5k(3), PEG5k(1)/2k(3), and PEG 5k(2)/2k(4) surfaces, respectively. The PEG5k(2)/2k(4) surface showed the greatest degree of inhibition of protein adsorption from the medium, suggesting that the inhibitory effect of nonspecific protein adsorption was the highest for this surface among those studied. The physicochemical properties of PEG surfaces described above indicate that PEG surfaces with higher immobilized PEG chain density have greater ability to repel proteins. Based on these results, it was concluded that shorter PEG, viz. an underbrushed layer to increase the PEG surface density, played a substantial role in minimizing nonspecific protein adsorption. Other workers have also proposed that PEG mixtures, which are polydisperse with respect to molecular weight, are more efficacious than single molecular weights. Mixed PEGs were shown to have greatest efficacy in steric stabilization of colloidal particles and in protein repellency.[34,35] The PEG5k-(2)/2k(4) surface with the highest PEG chain density was expected to have the highest cytophobicity.

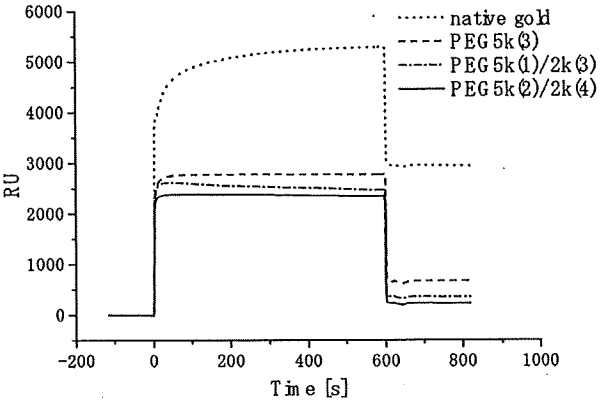

Figure 5. Sensorgrams of injection of serum-containing cell culture medium (EBM-2 medium to culture HUVEC) on native gold and each PEGylated surfaces. Flow rate, 10 μL/min; running buffer, PBS (pH 7.4, 0.15 M); sample injection volume, 100 μL.

2. Cell Culture Study. Gold surfaces were coated with PEG to inhibit nonspecific protein adsorption and were expected to act as cytophobic surfaces for subsequent cell patterning. The PEG-coated gold substrates were micropatterned by plasma etching ($N_2 + H_2$) through a metal mask pattern with ϕ100 μm circular holes separated by 300 μm (edge-to-edge distance), and cell culture dishes were then set onto these surfaces (2 × 2 cm). Microscopic images following seeding of HUVEC on the surfaces are shown in Figure 6. On PEG5k(3) surfaces with lower PEG chain density as suggested by physicochemical studies, seeded HUVEC showed disorganized cellular attachment regardless of micropatterned substrate (Figure 6a). On the other hand, the PEG5k(1)/2k(3) surface (Figure 6b) and PEG5k(2)/2k(4) surface (Figure 6c) showed patterned cell attachment due to the suggested higher PEG chain density compared with that of the PEG5k(3) surface, although cells that had overgrown beyond the pattern were still observed on PEG5k(1)/2k(3) surfaces. The results of cultivation of HUVECs for 1 week are shown in Figure 6d−f. Arrayed cellular attachment was observed only on the PEG5k-(2)/2k(4) surface (Figure 6f). In contrast, the HUVECs began to bridge across multiple islands on the PEG5k(1)/2k(3) surface (Figure 6e) and this bridging was more pronounced to form a complete cell sheet on the PEG5k(3) surface (Figure 6d). It is

(32) Harder, P.; Grunze, M.; Dahint, R.; Whitesides, G. M.; Laibinis, P. E. *J. Phys. Chem.* **1998**, *102*, 426.
(33) Zhu, B.; Eurell, T.; Gunawan, R.; Leckband, D. *J. Biomed. Mater. Res.* **2001**, *56*, 406.
(34) Stenkamp, V. S.; Berg, J. C. *Langmuir* **1997**, *13*, 3827.
(35) Pavey, K. D.; Olliff, C. J. *Biomaterials* **1999**, *20*, 885.

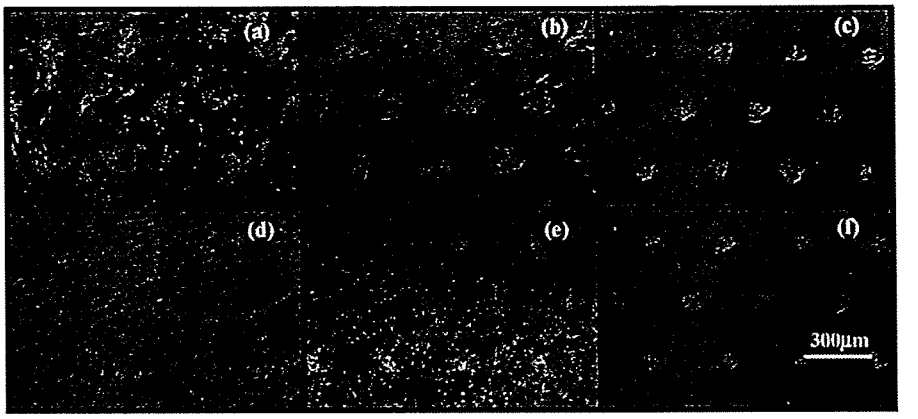

Figure 6. Microscopic image of cell seeding study. After 1 day of culture of HUVEC on micropatterned (a) PEG5k(3) surface, (b) PEG5k-(1)/2k(3) surface, and (c) PEG5k(2)/2k(4) surface. After 1 week of culture of HUVEC on micropatterned (d) PEG5k(3) surface, (e) PEG5k-(1)/2k(3) surface, and (f) PEG5k(2)/2k(4) surface.

clear that PEG chain density affects pattern recognition in cell attachment. The threshold density for HUVEC bridging seems to exist on the surface between PEG5k(3) and PEG5k(2)/2k(4). Cells overgrew beyond the pattern on weak protein-repellent surfaces. In addition, when overgrown cells grew sufficiently close together, bridging occurred between overgrown cellular patterns. Attached patterns eventually resulted in sheet formation. As described above, no pattern recognition of cell attachment was seen on the surfaces coated only with long-chain PEG (PEG5k(3)) because of its lower inhibitory effect on nonspecific protein adsorption. In contrast, cell array formation was observed by constructing long- and short-chain PEG mixed surfaces. Furthermore, PEG5k(2)/2k(4) surfaces showed the least non-specific cell attachment in contrast to some nonspecific cell attachment and bridging of cellular islands on PEG5k(1)/2k(3) surfaces. SPR results indicated that cell-adhesive proteins are greatly repelled on PEG5k(2)/2k(4) surfaces to promote pattern recognition of cell attachment. Some cell attachment between cellular islands was confirmed on PEG5k(3) and 5k(1)/2k(3) surfaces after 1 day in culture, and the attached cells extended toward each other and bridging occurred across cellular islands. Bridged cellular patterns grew everywhere on the surface and eventually formed a complete cell sheet. As the first cell attachment on the cytophobic region depends on the ability of the surface to repel protein, surfaces with lower PEG chain density (PEG5k(3) or PEG5k(1)/2k(3)) resulted in cell attachment and cell sheet formation. Thus, the results of the cell culture study agreed well with the surface properties, suggesting that PEG chain density played a critical role in micropatterned cell attachment.

Conclusions

To gain insight into the design of cellular microenvironments, we examined the micropatterning of endothelial cells on microfabricated gold substrates coated with PEG brushes in terms of the relationship between PEG chain density and cellular attachment. A PEG-brushed layer was constructed on a gold substrate using PEG with a mercapto group at the chain end. After treatment with longer chain PEG with a molecular weight of 5000, shorter chain PEG (2000) was introduced onto the gold substrate to modulate the chain density. In this way, PEGylated surfaces with different chain densities were produced, and subsequent micropatterning was achieved by plasma etching through a micropatterned metal mask. The results indicated that cell pattern formation was strongly dependent on both the PEG chain density and the extent of protein adsorption, as evidenced by physicochemical and biological characterization of PEGylated surfaces using SPR, QCM, and static/dynamic contact angle measurements. Cell micropatterning showed long-term retention only on the surfaces with greater disparity between cytophobic and cytophilic regions. Notably, a PEG chain density sufficiently high to inhibit outgrowth of endothelial cells beyond the cytophilic gold region to the cytophobic PEGylated region could be obtained only on the mixed PEG chain-tethered surface, which achieved almost complete prevention of nonspecific protein adsorption. These observations clearly indicated that shorter PEG, viz. an underbrushed PEG layer to increase the PEG surface density, played a substantial role in minimizing nonspecific protein adsorption and long-term maintenance of the active cell pattern. It should be noted that the precise control of surface properties in single-molecule order directly affected micropatterned cellular attachment. Therefore, we envision the cellular micropatterning technique presented here becoming a valuable tool for the control of cell−surface and cell−cell interactions on a micrometer scale and to evaluate local effects of engineered microenvironments on cellular behavior. The surface fabrication technique studied here is a promising technology for the development of tissue/cell-based biosensors and in the field of tissue engineering.

Acknowledgment. Microfabrication using the plasma etching technique was conducted at the National Institute for Materials Science (NIMS), Japan, with assistance from Dr. Y. Horiike. Financial support for this work was partly provided by Special Coordination Funds for Promoting Science and Technology and also supported by Research Promotion Bureau under contract nos. 15-99 and 15-396, both from the Ministry of Education, Culture, Sports, Science, and Technology (MEXT), Japan. Part of this work was also supported financially by a Grant-in-Aid for Research on Health Sciences for Drug Innovation (KH71066), Ministry of Health, Labor, and Welfare of Japan, and The New Energy and Industrial Technology Development Organization (NEDO).

LA0624384

J|A|C|S
COMMUNICATIONS

Published on Web 04/05/2007

A Protein Nanocarrier from Charge-Conversion Polymer in Response to Endosomal pH

Yan Lee,[†] Shigeto Fukushima,[‡] Younsoo Bae,[†,§] Shigehiro Hiki,[‡,||] Takehiko Ishii,[#] and Kazunori Kataoka*[,†,‡,§,||,#]

Division of Clinical Biotechnology, Center for Disease Biology and Integrative Medicine, Graduate School of Medicine, Department of Materials Engineering, Center for NanoBio Integration, CREST, Japan Science and Technology Corporation, and Department of Bioengineering, University of Tokyo, 7-3-1 Hongo, Bunkyo-ku, Tokyo 113-0033, Japan

Received February 14, 2007; E-mail: kataoka@bmw.t.u-tokyo.ac.jp

Smart polymers, whose characteristics change in response to an external signal, such as electric potential, magnetic field, temperature, light, and pH, etc., are spotlighted in various research fields including analytical chemistry, tissue engineering, and drug delivery.[1] Especially, the smart polymers, which are sensitive to biosignals, that is, reductive potential[2] or pH, are very attractive in the drug delivery field requiring selective controlled-release. Some pH-sensitive polymers are even facilitating the endosomal escape of drugs by a membrane interaction and/or an increase in the local osmotic pressure.[3]

pH-Sensitive polymers developed so far that release drugs in the endosomal component use acetal, hydrazone, and orthoester bonds, etc.[4] Although they showed a selective degradation in the endosome, their drug release in response to pH was relatively passive and slow. A more active and prompt response to a small pH drop is needed for more effective drug delivery, for example, the specific release in the early endosome.

Citraconic anhydride is an α-methyl derivative of maleic anhydride, which can be used to mask the charge of proteins. As shown in Scheme 1, amide bonds are formed from the reaction between primary amines and citraconic anhydride. The resulting amides have negative charges owing to the carboxylate groups at the end. The citraconic amide is stable at both neutral and basic pH, but it becomes unstable at acidic pH and promptly degrades back into the cationic primary amine. It has been reported that the citraconic amide degrades around pH 5.[5] Therefore, we considered that the citraconic amide could provide a pH-dependent degradability to the polymers that can be selectively functionalized during the early endosome in a cell. Because the degradation was directly related to the charge-conversion, it could also provide an abrupt change in the interaction with counter-ions.

In this study, we synthesized a block copolymer with combtype side groups of the citraconic amide and characterized their physicochemical properties such as the degree of degradability and the charge conversion. With this polymer, we also developed a novel nanocontainer that can promptly release its protein cargo by generating a repulsive electrostatic force owing to the charge-conversion at the endosomal pH.

The synthesis of the diblock copolymer, poly(ethylene glycol)-poly[(*N*′-citraconyl-2-aminoethyl)aspartamide] (PEG-pAsp(EDA-Cit)) (**4**) is illustrated in Scheme 1. The diblock copolymer **2** was synthesized as previously reported.[6] Briefly, the ring-opening polymerization of β-benzyl-L-aspartate *N*-carboxy-anhydride (BLA-NCA) was initiated by the terminal primary amino group of α-methoxy-ω-amino poly(ethylene glycol) (M_n = 12 000) (**1**), and the reaction produced **2**. The prepared **2** was further modified into PEG-poly[(2-aminoethyl)aspartamide] (**3**) by aminolysis with excess ethylenediamine. Finally, **4** was synthesized from **3** and the citraconic anhydride in the pyridine solvent. The detailed synthetic procedures are described in the Supporting Information.

Scheme 1. Synthesis of PEG-pAsp(EDA-Cit): (a) BLA-NCA/DMF; (b) Ethylenediamine/DMF; (c) Citraconic Anhydride (or Succinic Anhydride)/pyridine

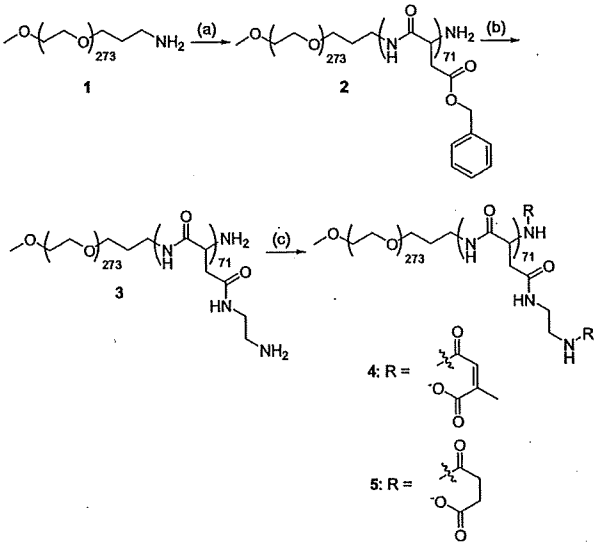

The pH-dependent degradation rates of the citraconic amide of **4** are shown in Figure 1. The degradation rate was calculated by measurement of the primary amine concentration in the polymer at 37 °C. The fluorescamine method was used for the quantification of the amine concentration.[7] In the meantime, PEG-pAsp(EDA-Suc) (**5**) was synthesized as the negative control by mixing **4** with succinic anhydride instead of citraconic anhydride. Although **5** has a structure similar to **4**, **5** does not degrade under acidic pH conditions. The experiments showed that approximately 80% of the citraconic amides was degraded in the acetate buffer (pH 5.5) within 1 h, while 60% of the citraconic amides remained intact in the phosphate buffer (pH 7.4) even after 5 h. No degradation was observed in the case of the succinic amides under both pH conditions.

We previously reported that the formation and characterization of the PIC micelles between the PEG-polyaspartate (PEG-pAsp) and lysozyme, of which the isoelectric point occurs at pH 10.[8]

† Center for Disease Biology and Integrative Medicine, University of Tokyo.
‡ Department of Materials Engineering, University of Tokyo.
§ Center for Nanobio Integration, University of Tokyo.
|| CREST, Japan Science and Technology Corporation.
Department of Bioengineering, University of Tokyo.

10.1021/ja071090b CCC: $37.00

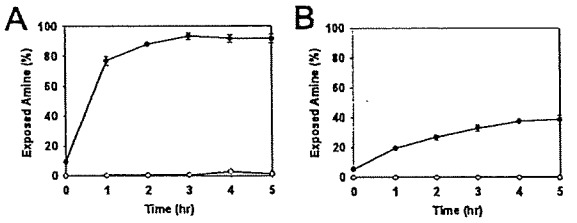

Figure 1. The degradation of citraconic amide (●) and succinic amide (○) in 4 and 5 at pH 5.5 (A) and pH 7.4 (B). The data are expressed as mean values (± standard deviation) of three experiments.

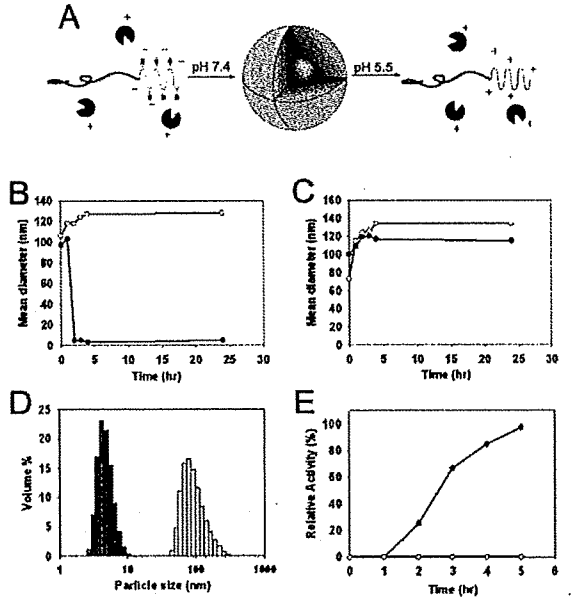

Figure 2. Formation and dissociation of the PIC micelles: (A) schematic diagram for the formation and dissociation of the PIC micelles; the time course of the mean diameter of the PIC micelles of (B) PEG-pAsp(EDA-Cit) and (C) PEG-pAsp(EDA-Suc); (D) the DLS histogram of the PIC micelles at 0 h (white) and at 2 h (gray) at pH 5.5; and (E) the relative lysozyme activity of the PIC micelles. The black dots (●) represent the data at pH 5.5 and the white dots (○) are at pH 7.4.

Following the experimental protocols, the PIC micelles were prepared by mixing **4** and the lysozyme. The pH-dependent stability of the micelles was analyzed by dynamic light scattering (DLS) measurements. The measurements demonstrated that the PIC micelles were successfully formed. More notably, it also suggested that these micelles would be destabilized at the endosomal pH by the degradation of the citraconic amides in **4** accompanied by the charge conversion from negative to positive (Figure 2A).

Figure 2B demonstrates that the size of the micelles prepared from **4** and the lysozymes was stabilized with a diameter of about 130 nm at pH 7.4 even after incubation at 37 °C for 24 h. However, the PIC micelles were promptly dissociated at pH 5.5 within 2 h. The pH dependent profiles of the PIC micelles from **5** and the lysozymes are shown in Figure 2C. As expected, the succinic amide-based micelles were stable at both pH values after 24 h. Figure 2D shows the size distribution of the citraconic amide-based micelles before and after the dissociation. The micelles showed a unimodal size distribution before the dissociation. The distribution around 4.8 nm after a 2-hr incubation resulted from the single lysozyme molecule.[8]

Figure 2E shows the activity of the lysozyme released from the PIC micelles. The lysozyme activity was measured by the well-known method using the *Micrococcus luteus* cell suspension.[9] The relative activity is expressed as a percentage of the free-lysozyme activity. Because the activity depends on the pH, the free-lysozyme activity at each pH was used for the calculation of relative activity.

At pH 7.4, no lysozyme activity was observed for over 5 h. However, at pH 5.5, the PIC micelles showed a lysozyme activity after 2 h, and it increased and reached 97% of the free-lysozyme activity after 5 h. Interestingly, it took 3 h more to observe the full lysozyme activity after the dissociation of the micelles. Considering the fact that the micelles dissociated within 2 h, it is suggested that there is a weak interaction between the lysozyme and block copolymer chains at least 3 h after the dissociation of the micelles. Because the direct contact between lysozyme and the bacterial cell wall is required for the full activity, PEG chain bound to lysozyme, even though the binding is very weak, can reduce the lysozyme activity. After 80% degradation, **4** cannot form the PIC micelles with lysozyme, but it can still repress the lysozyme activity below 5% (data not shown). Nevertheless, it was confirmed that the citraconic amide-based micelles can selectively dissociate and release the lysozyme while maintaining its enzymatic activity by responding to the change in pH.

In summary, we synthesized the charge-converting block copolymer using the citraconic amide as a pH-sensitive charge masking group. The citraconic amide-based block copolymer was selectively degraded in response to the endosomal pH and formed PIC micelles with the cationic model protein, that is, the lysozyme. Most notably, the micelles selectively released the active lysozyme promptly by sensing the change in pH corresponding to the acidic conditions in the intracellular endosomal compartments. Therefore, it was concluded that our stimuli-sensitive block copolymers are promising designs for future drug and gene delivery systems.

Acknowledgment. This work was supported by the Core Research for Evolutional Science and Technology (CREST) from the Japan Science and Technology Agency (JST) as well as by Special Coordination Funds for Promoting Science and Technology from the Ministry of Education, Culture, Sports, Science and Technology of Japan (MEXT).

Supporting Information Available: Materials and methods, the temperature-depending degradation rate of the polymer and dissociation rate of the PIC micelles. This material is available free of charge via the Internet at http://pubs.acs.org.

References

(1) (a) Idota, N.; Kikuchi, A.; Kobayashi, J.; Sakai, K.; Okano, T. *Adv. Mater.* **2005**, *17*, 2723–2727. (b) Roy, I.; Gupta, M. N. *Chem. Biol.* **2003**, *10*, 1161–1171. (c) Schmaljohann, D. *Adv. Drug Delivery Rev.* **2006**, *58*, 1655–1670.

(2) (a) Lee, Y.; Koo, H.; Jin, G.; Mo, H.; Cho, M. Y.; Park, J.; Choi, J. S.; Park, J. S. *Biomacromolecules* **2005**, *6*, 24–26. (b) Miyata, K.; Kakizawa, Y.; Nishiyama, N.; Harada, A.; Yamasaki, Y.; Koyama, H.; Kataoka, K. *J. Am. Chem. Soc.* **2004**, *126*, 2355–2361.

(3) (a) Oishi, M.; Kataoka, K.; Nagasaki, Y. *Bioconjugate Chem.* **2006**, *17*, 677–688. (b) Boussif, O.; Lezoualc'h, F.; Zanta, M. A.; Mergny, M. D.; Scherman, D.; Demeneix, B.; Behr, J. P. *Proc. Natl. Acad. Sci. U.S.A.* **1995**, *92*, 7297–7301.

(4) (a) Murthy, N.; Thng, Y. X.; Schuck, S.; Xu, M. C.; Fréchet, J. M. J. *J. Am. Chem. Soc.* **2002**, *124*, 12398–12399. (b) Bae, Y.; Fukushima, S.; Harada, A.; Kataoka, K. *Angew. Chem., Int. Ed.* **2003**, *42*, 4640–4643. (c) Heller, J.; Barr, J.; Ng, S. Y.; Abdellauoi, K. S.; Gurny, R. *Adv. Drug Delivery Rev.* **2002**, *54*, 1015–1039.

(5) Shetty, J. K.; Kinsella, J. E. *Biochem. J.* **1980**, *191*, 269–272.

(6) Fukushima, S.; Miyata, K.; Nishiyama, N.; Kanayama, N.; Yamasaki, Y.; Kataoka, K. *J. Am. Chem. Soc.* **2005**, *127*, 2810.

(7) Udenfriend, S.; Stein, S.; Bohlen, P.; Dairman, W.; Leimgruber, W.; Weigele, M. *Science* **1972**, *178*, 871–872.

(8) Harada, A.; Kataoka, K. *Macromolecules* **1998**, *31*, 288–294.

(9) Harada, A.; Kataoka, K. *J. Am. Chem. Soc.* **1999**, *121*, 9241–9242.

JA071090B

Improvement of cancer-targeting therapy, using nanocarriers for intractable solid tumors by inhibition of TGF-β signaling

Mitsunobu R. Kano*†‡, Younsoo Bae‡§, Caname Iwata*¶, Yasuyuki Morishita*, Masakazu Yashiro‖, Masako Oka*, Tomoko Fujii*, Akiyoshi Komuro*, Kunihiko Kiyono*, Michio Kaminishi¶, Kosei Hirakawa‖, Yasuyoshi Ouchi†, Nobuhiro Nishiyama§**, Kazunori Kataoka‡§**††, and Kohei Miyazono*‡‡

Departments of *Molecular Pathology, †Geriatrics, ¶Gastrointestinal Surgery, and §Center for Disease Biology and Integrative Medicine, Graduate School of Medicine; **Department of Materials Engineering, Graduate School of Engineering; and ‡Center for Nano-Bio Integration, University of Tokyo, Tokyo 113-0033 Japan; and ‖Department of Surgical Oncology, Osaka City University Graduate School of Medicine, Osaka 545-8585, Japan

Communicated by Tadatsugu Taniguchi, University of Tokyo, Tokyo, Japan, December 28, 2006 (received for review December 25, 2006)

Transforming growth factor (TGF)-β plays a pivotal role in regulation of progression of cancer through effects on tumor microenvironment as well as on cancer cells. TGF-β inhibitors have recently been shown to prevent the growth and metastasis of certain cancers. However, there may be adverse effects caused by TGF-β signaling inhibition, including the induction of cancers by the repression of TGF-β-mediated growth inhibition. Here, we present an application of a short-acting, small-molecule TGF-β type I receptor (TβR-I) inhibitor at a low dose in treating several experimental intractable solid tumors, including pancreatic adenocarcinoma and diffuse-type gastric cancer, characterized by hypovascularity and thick fibrosis in tumor microenvironments. Low-dose TβR-I inhibitor altered neither TGF-β signaling in cancer cells nor the amount of fibrotic components. However, it decreased pericyte coverage of the endothelium without reducing endothelial area specifically in tumor neovasculature and promoted accumulation of macromolecules, including anticancer nanocarriers, in the tumors. Compared with the absence of TβR-I inhibitor, anticancer nanocarriers exhibited potent growth-inhibitory effects on these cancers in the presence of TβR-I inhibitor. The use of TβR-I inhibitor combined with nanocarriers may thus be of significant clinical and practical importance in treating intractable solid cancers.

angiogenesis | gastric cancer | molecular targeting therapy | pancreatic cancer

Chemotherapy that uses nanocarriers has been developed to improve the clinical treatment of solid tumors by obtaining high accumulation of drugs in tumor tissues but limited accumulation in normal organs. Doxil (1), a liposomal adriamycin (ADR), is one such drug that has already been used clinically (2). Doxil has exhibited therapeutic effects on some cancers with hypervascular characteristics (3, 4), including Kaposi sarcoma and ovarian cancers. Another promising formulation of nanocarriers is polymeric micelles (5, 6), which are already being used in clinical trials (7, 8).

However, despite the urgent need for effective chemotherapy for intractable solid tumors, including pancreatic adenocarcinoma (9) and diffuse-type gastric carcinoma (10), nanocarriers of any design have not been successful yet in exhibiting significant therapeutic effects on these cancers. Pancreatic cancer is the fourth leading cause of cancer-related death in the United States and the fifth in Japan (9), and the median survival period of patients who suffer from advanced pancreatic adenocarcinoma is still extremely short (≈6 months), despite recent progress in development of conventional chemotherapies (11). Although cancer cells derived from these tumors are sufficiently sensitive *in vitro* to conventional anticancer agents such as ADR (12), most of these agents have failed to exhibit sufficient therapeutic effects *in vivo*, regardless of formulation, whether encapsulated in nanocarriers or not. The theoretical basis of the specific accumulation of nanocarriers in tumor tissues is leakiness of tumor vessels to the macromolecular agents, termed the "enhanced permeability and retention (EPR) effect," which was demonstrated and named by Maeda *et al.* (13, 14). The major obstacles to treatment of these cancer cells could thus be insufficient EPR effect because of certain characteristics of their cancer microenvironment, including hypovascularity and thick fibrosis (15, 16). However, methods of regulating this effect have not been well investigated.

Transforming growth factor (TGF)-β signaling plays a pivotal role in both the regulation of the growth and differentiation of tumor cells and the functional regulation of tumor interstitium (17). Because TGF-β is a multifunctional cytokine that inhibits the growth of epithelial cells and endothelial cells and induces deposition of extracellular matrix, inhibition of TGF-β signaling in cancer cells and fibrotic components has been expected to facilitate the effects of anticancer therapy. TGF-β binds to type II (TβR-II) and type I receptors (TβR-I), the latter phosphorylates Smad2 and −3. Smad2 and −3 then form complexes with Smad4, translocate into the nucleus, and regulate the transcription of target genes (18). Several small-molecule TβR-I inhibitors have been reported to prevent metastasis of some cancers (19). However, there may be adverse effects of TGF-β inhibition, including potential progression of some cancers because of the repression of TGF-β-mediated growth inhibition of epithelial cells (20).

In this study, we show that administration of the small-molecule TβR-I inhibitor (LY364947) (21) at a low dose, which could minimize the potential side effects of TβR-I inhibitor, can alter the tumor microenvironment and enhance the EPR effect. This effect of low-dose TβR-I inhibitor was demonstrated with two of nanocarriers, i.e., Doxil and a polymeric micelle incorporating ADR (micelle ADR) that we have recently developed (22) [supporting information (SI) Fig. 7]. The present findings strongly suggest that our method, which uses a combination of

Author contributions: M.R.K., K. Kataoka, and K.M. designed research; M.R.K., Y.B., C.I., Y.M., M.O., T.F., A.K., and K. Kiyono performed research; M.Y. and K.H. contributed new reagents/analytic tools; M.R.K., Y.B., C.I., M.K., Y.O., N.N., K. Kataoka, and K.M. analyzed data; and M.R.K., N.N, K. Kataoka, and K.M. wrote the paper.

The authors declare no conflict of interest.

Freely available online through the PNAS open access option.

Abbreviations: ADR, adriamycin; EPR, enhanced permeability and retention; PECAM, platelet/endothelial cell adhesion molecule; TβR-I, type I transforming growth factor β receptor.

††To whom correspondence may be addressed at: Department of Material Engineering, Graduate School of Engineering, University of Tokyo, Tokyo 113-8656, Japan. E-mail: kataoka@bmw.t.u-tokyo.ac.jp.

‡‡To whom correspondence may be addressed. E-mail: miyazono-ind@umin.ac.jp.

This article contains supporting information online at www.pnas.org/cgi/content/full/0611660104/DC1.

www.pnas.org/cgi/doi/10.1073/pnas.0611660104

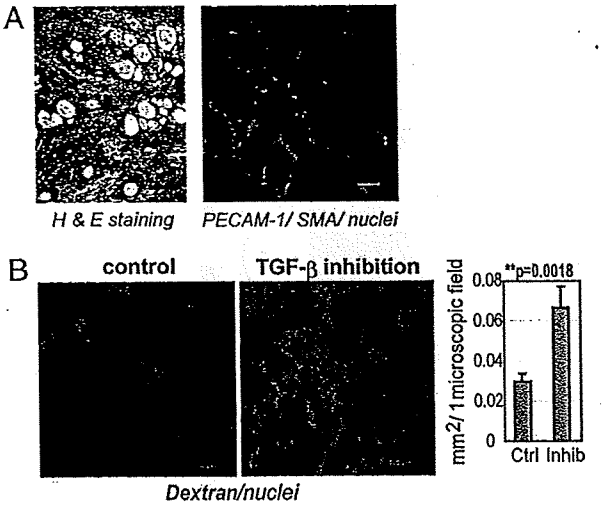

Fig. 1. Histology of BxPC3 xenograft and effects of low-dose TβR-I inhibitor. (*A*) The histology of the TGF-β-nonresponsive BxPC3 xenograft, used as a model of poorly differentiated pancreatic adenocarcinoma, shown in H&E staining and immunohistochemistry. Examination revealed nests of tumor cells in gland-like structures, with areas rich in fibrotic components (filled by α-smooth muscle actin (SMA)-positive myofibroblasts, shown in red) between them. The tumor tissue also includes some PECAM-1-positive vessels (shown in green) in the interstitium, although almost no vasculature was observed inside the nests of tumor cells. (*B*) Dextran leakage. At 24 h after administration of low-dose TβR-I inhibitor (1 mg/kg i.p.), i.v.-administered dextran of 2 MDa (50 nm in hydrodynamic diameter) exhibited broader distribution with 1 mg/kg TβR-I inhibitor (*Right*) than in the control (*Left*), which was quantified and shown in the graph ($n = 12$). Error bars in the graphs represent standard errors, and *P* values were calculated by Student's *t* test. Ctrl, control; Inhib, inhibitor. (Scale bars, 100 μm.)

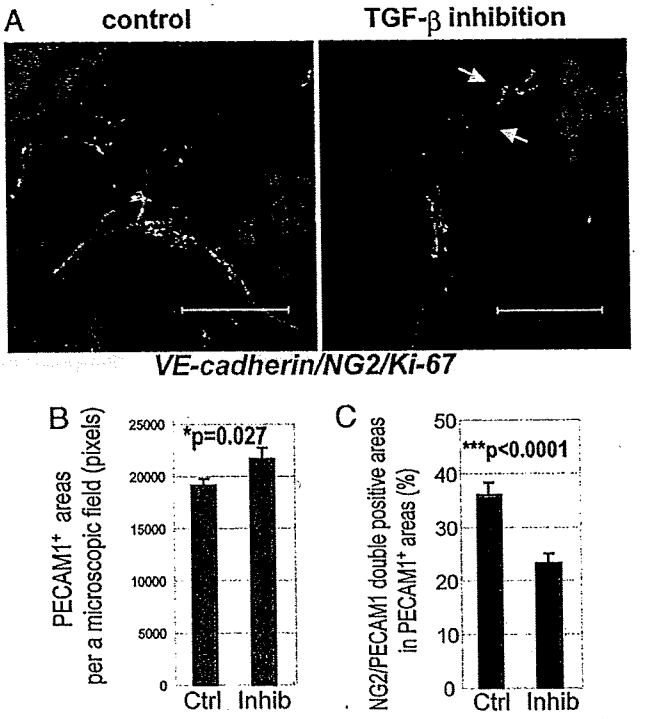

Fig. 2. Morphological changes in cancer neovasculature at 24 h after administration of low-dose TβR-I inhibitor. (*A*) Immunostaining of the tumor neovasculature. NG2-positive pericytes (shown in red) were dissociated (yellow arrows in *Right*) from VE-cadherin-positive endothelium (shown in green) after TβR-I inhibitor treatment for 24 h. (Scale bars, 50 μm.) (*B* and *C*) Areas of PECAM-1-positive endothelium (*B*) and pericyte-coverage (*C*) were quantified ($n = 40$) and are shown in the graphs. Error bars in the graphs represent standard errors, and *P* values were calculated by Student's *t* test. Ctrl, control; Inhib, inhibitor.

low-dose small molecule TβR-I inhibitor and long-circulating nanocarriers, is a promising way to treat intractable cancers.

Results

We used the xenografted BxPC3 human pancreatic adenocarcinoma cell line in nude mice as a disease model (Fig. 1). BxPC3 cells do not respond to TGF-β, because of lack of functional Smad4. Hematoxylin/eosin (H&E) staining of tumor tissue in this model (Fig. 1*A Left*) revealed poorly differentiated histology, with a certain number of blood vessels and thick fibrotic tissue in the interstitium. There was, however, almost no vasculature inside of tumor cell nests (Fig. 1*A Right*). This model thus represents the histological characteristics of some intractable solid tumors.

Systemic administration of low-dose TβR-I inhibitor in this model significantly altered the characteristic of tumor vasculature at 24 h after administration. We investigated the functional aspects of the effects of low-dose TβR-I inhibitor, using i.v.-administered large-molecule dextran of 2 MDa with a hydrodynamic diameter of 50 nm (23, 24), which is equivalent to the common sizes of nanocarriers (Fig. 1*B*). Although dextran of this molecular size for the most part remained in the intravascular space in the control condition, as reported in ref. 24, the use of TβR-I inhibitor resulted in a far broader distribution of this macromolecule around the tumor neovasculature. These findings suggest that low-dose TβR-I inhibitor can maintain blood flow in the tumor vasculature and simultaneously induce extravasation of macromolecules.

To investigate the mechanisms of effect of TβR-I inhibitor on the neovasculature, we analyzed the changes in three major components of tumor vasculature, i.e., endothelium, pericytes (Fig. 2), and basement membrane (SI Fig. 8), at 24 h after administration of TβR-I inhibitor. The areas of vascular endothelial cells stained by platelet/endothelial cell adhesion molecule (PECAM)-1 increased slightly with TβR-I inhibitor treatment (Fig. 2*B*). Although pericyte-coverage of endothelium has been reported to be incomplete in tumors (25), coverage of the endothelium by pericytes, which were determined as NG2-positive perivascular cells, was further decreased by the TβR-I inhibitor treatment. This finding was confirmed by comparing the ratios of PECAM-1/NG2-double-positive areas to PECAM-1-positive areas (Fig. 2*C*). On the other hand, vascular basement membrane, which was determined by staining with collagen IV, did not differ significantly in the presence or absence of TβR-I inhibitor (SI Fig. 8). We also examined the vasculature in normal organs and found that it was not affected by TβR-I inhibitor in terms of permeability of 2-MDa dextran and morphology on immunostaining (SI Fig. 9).

We next examined the effects of i.p. administration of small-molecule TβR-I inhibitor at a low dose (1 mg/kg) on TGF-β signaling, by determining phosphorylation of Smad2 (SI Figs. 10 and 11). Because it is a small-molecule agent, TβR-I inhibitor transiently suppressed phosphorylation of Smad2. In nucleated blood cells, phosphorylation of Smad2 was significantly suppressed at 1 h after administration of TβR-I inhibitor, but it gradually recovered toward 24 h. In contrast, phosphorylation of Smad2 in tumor cells and most interstitial cells was not suppressed even 1 h after administration, whereas a higher dose (25 mg/kg) of TβR-I inhibitor inhibited Smad2 phosphorylation in most tumor cells. Accordingly, the extent of fibrosis in cancer xenografts treated with low-dose TβR-I inhibitor did not differ

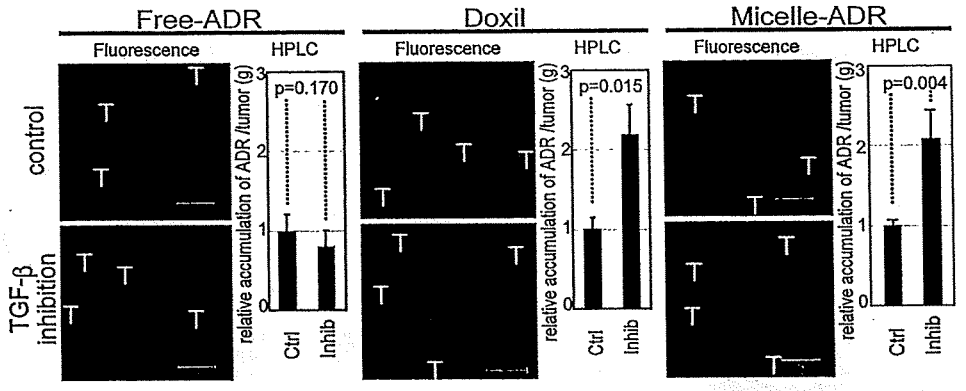

Fig. 3. Biodistribution of ADR in the BxPC3 model. The biodistribution of ADR was investigated in the BxPC3 model by fluorescence examination (T indicates nests of tumor cells in tumor tissues) and by HPLC. The distributions of Doxil, micelle ADR, and free ADR at 8 mg/kg with and without TβR-I inhibitor at 1 mg/kg were examined 24 h after administration. Enhancement of drug accumulation in tumor was specifically observed with TβR-I inhibitor with Doxil and micelle ADR. Error bars in the graphs represent standard errors, and *P* values were calculated by Student's *t* test. Ctrl, control; Inhib, inhibitor.

from that in the control (SI Fig. 12). On the other hand, low-dose TβR-I inhibitor specifically suppressed the phosphorylation of Smad2 in vascular endothelium (SI Fig. 11*B*). These findings suggest that the use of small-molecule TβR-I inhibitor at low doses is advantageous for limiting adverse effects.

We thus hypothesized that low-dose TβR-I inhibitor may enhance the accumulation of nanocarriers, the molecular sizes of which are similar to 2-MDa dextran, in hypovascular solid tumors. We used two nanocarriers to test this hypothesis: Doxil (26), a liposomal ADR, and a core–shell type polymeric micelle-encapsulating ADR (micelle ADR) that we developed (22). The latter is a micellar nanocarrier consisted of block copolymers in which ADR is conjugated to the PEG chain through an acid–labile linkage. This drug carrier releases free ADR molecules selectively in acidic conditions, e.g., in intracellular endosomes and lysosomes (SI Fig. 7). We tested the effects of i.p. administration of TβR-I inhibitor with i.v. administration of Doxil or micelle ADR at 8 mg/kg on size-matched xenografts of BxPC3 cells, which are ADR-sensitive *in vitro* (12). Conventional ADR without drug carriers (free ADR), a small-molecule compound of MW 543.52, was also used for comparison. We first examined the distribution of ADR molecules in tumor tissues by using confocal imaging of fluorescence of ADR and HPLC (Fig. 3). The fluorescence of ADR molecules in micelle ADR is detectable only when ADR molecules are released from the micelle, whereas that in Doxil is detectable even when it is encapsulated in the liposome. The total amount of accumulated ADR, the sum of that in cancer cells and the cancer microenvironment, is measured by HPLC, which detects ADR molecules with and without drug carriers. Administration of TβR-I inhibitor with the nanocarriers yielded significant enhancement of intratumoral accumulation of ADR molecules. Because TβR-I inhibitor did not increase the accumulation of free ADR, we suspected that only macromolecules would be benefited by the use of TβR-I inhibitor through enhancement of EPR effect.

We then examined the growth-inhibitory effects of these anticancer drugs with and without TβR-I inhibitor on size-matched BxPC3 xenografts. As shown in Fig. 4*A*, the growth curves of the BxPC3 xenografts confirmed the findings for the distribution of ADR molecules. None of free ADR, Doxil, micelle ADR as monotherapy, or free ADR with TβR-I inhibitor significantly reduced tumor growth. In contrast, ADR encapsulated in nanocarriers exhibited significant effects on the growth of tumor when combined with TβR-I inhibitor (see *SI List* for statistical study).

Because micelle ADR was more effective than Doxil (as shown in Figs. 3 and 4*A*), and the maximum tolerated dose of micelle ADR is far higher than one shot of 8 mg/kg (22, 26) (the dose in Fig. 4*A*), we further tested the growth-inhibitory effects of an increased dose of micelle ADR combined with TβR-I inhibitor (Fig. 4*B*). When micelle ADR or free ADR was

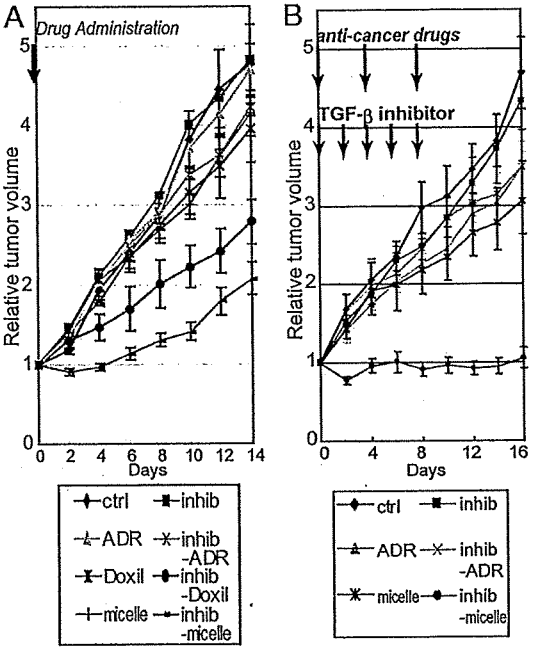

Fig. 4. Effects of TβR-I inhibitor on anti-tumor activity of nanocarriers, incorporating ADR in the BxPC3 model. (*A*) Free ADR, liposomal ADR (Doxil), micelle ADR (micelle) or vehicle control (ctrl) was administered i.v. in a single bolus with and without TβR-I inhibitor (inhib) i.p. to xenografted mice in which tumors had been allowed to grow for a few weeks before treatment ($n = 5$). Relative tumor sizes were measured every second day and are shown as a growth curve with bars showing standard errors. Only nanocarriers administered together with TβR-I inhibitor exhibited significant reduction of growth compared with the control. (*B*) Growth curve study with an increased dose of micelle ADR. With the day of initiation of drug administration designated day 0, anticancer drugs were administered i.v. on days 0, 4, and 8 with and without i.p. TβR-I inhibitor on days 0, 2, 4, 6, and 8. Further growth-inhibitory effect was observed with an increase in dose of micelle ADR. (Results of multivariate ANOVA study are shown in *SI List*.)

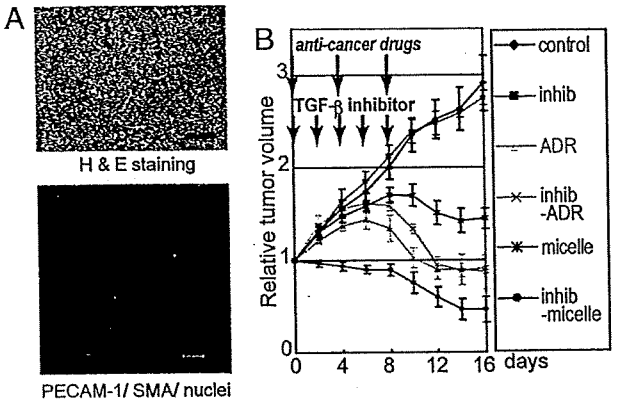

Fig. 5. Growth-curve study in the MiaPaCa-2 pancreatic cancer xenograft model. (*A*) TGF-β-nonresponsive MiaPaCa-2 cell xenografts exhibited an undifferentiated pattern of histology on H&E staining (*Upper*), with rich SMA-positive fibrotic tissue (show in red in *Lower*) and much less PECAM-1-positive vasculature (shown in green) compared with the BxPC3 model. (*B*) The same experimental protocol as in Fig. 4*B* was used in the model, and the effectiveness of the use of TβR-I inhibitor was confirmed. Inhib, inhibitor; micelle, micelle-ADR. (Results of multivariate ANOVA for the growth-curve studies are shown in *SI List*.)

administered on days 0, 4, and 8, with and without TβR-I inhibitor, only micelle ADR administered together with TβR-I inhibitor exhibited nearly complete growth-inhibitory effect on the tumor in this model. We therefore used this regimen in the following experiments.

The efficacy of combined treatment was further confirmed by using micelle ADR in two other animal models of pancreatic adenocarcinoma. We used size-matched xenograft models of MiaPaCa-2 and Panc-1 cell lines, which are both ADR-sensitive *in vitro* (12) (Fig. 5 and SI Figs. 13 and 14). MiaPaCa-2 is nonresponsive to TGF-β signaling because of TβR-II deficiency, whereas Panc-1 has no deficiency in TGF-β signaling components and responds to TGF-β. On histological examination, the xenografts of MiaPaCa-2 and Panc-1 exhibited similar undifferentiated pattern with scattered cancer cells, rich fibrous tissue, and sparse vasculature distributed homogeneously, unlike that of BxPC3 xenografts (Fig. 5*A* and SI Fig. 14*A*). Use of low-dose TβR-I inhibitor in these models again significantly enhanced the growth-inhibitory effects of micelle ADR (see Fig. 5*B*, SI Fig. 14*B*, and *SI List* for statistical analyses). Effects of free ADR were again not enhanced by TβR-I inhibitor, although the drug itself exhibited some degree of growth-inhibitory effect on the MiaPaCa-2 xenografts. Analysis of the biodistribution of ADR molecules (SI Figs. 13 and 14 *C* and *D*) confirmed the effects of TβR-I inhibitor on accumulation of micelle ADR in these cancer models.

We also tested the growth-inhibitory effect of TβR-I inhibitor and micelle ADR in an orthotopic model of the OCUM-2MLN cell line, which responds to TGF-β (27) (Fig. 6). OCUM-2MLN was derived from a patient with another intractable solid tumor, diffuse-type gastric cancer. The cancer cells were implanted in the gastric wall of nude mice and allowed to grow *in situ* for 2 weeks, leading to formation of hypovascular and fibrotic tumors in the gastric wall (Fig. 6*A*). Tumor area (framed by arrowheads in Fig. 6*B*, *Left*) was measured before the initiation of drug administration, and tumor growth was evaluated by calculating the relative tumor area at day 16 by measuring tumor area again (Fig. 6*B*, *Right*). Significant reduction of tumor growth was again observed only in the mice treated with TβR-I inhibitor and micelle ADR. The distribution of ADR, as detected by fluorescence, confirmed this growth-inhibitory effect (data not shown). These findings suggest that the use of TβR-I inhibitor may enhance the accumulation of nanocarriers in hypovascular solid tumors.

Finally, we examined whether low-dose TβR-I inhibitor increases EPR effect specifically in tumor tissues and not in normal organs. Although nanocarriers were originally designed to decrease the drug accumulation in normal organs, it is important to determine whether use of TβR-I inhibitor exacerbates their side effects (SI Fig. 15). In liver, spleen, kidney, blood, and heart, accumulation of ADR as determined by HPLC was not significantly increased by TβR-I inhibitor (SI Fig. 15 *A* and *B*). Neither dermatitis nor phlebitis around the tail veins was exacerbated by addition of TβR-I inhibitor (SI Fig. 15*C*). In addition, the weight

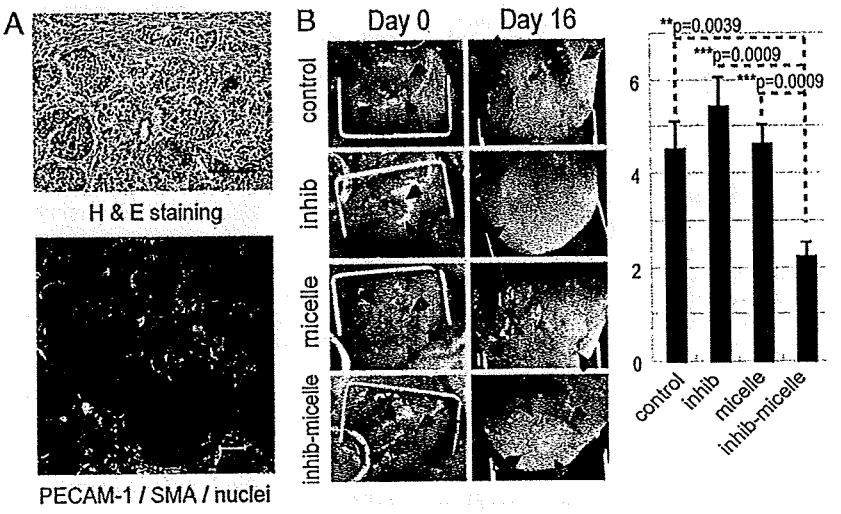

Fig. 6. Effects of TβR-I inhibitor administered together with micelle ADR in an orthotopic diffuse-type gastric cancer model. OCUM-2MLN, a human diffuse-type gastric cancer cell line, was inoculated into the gastric wall of nude mice ($n = 5$). Two weeks after inoculation, the cancer tissues exhibited diffuse-type histology on H&E staining (*A Upper*) with sparse formation of blood vessels (PECAM-1 staining, shown in green) (*A Lower*). The sizes of tumors on the gastric wall were measured based on tumor areas (*B Left*), and the values on day 16 were divided by those on day 0, the day of initiation of drug administration, to obtain relative tumor areas. Relative tumor areas are shown with bars for standard errors (*B Right*). TβR-I inhibitor significantly reduced tumor growth in this model, as well. *P* values were calculated by Student's *t* test. Inhib, inhibitor; micelle, micelle-ADR.

of mice that were treated with micelle ADR was not significantly affected by TβR-I inhibitor (data not shown). These findings in normal organs strongly suggest that low-dose TβR-I inhibitor enhances EPR effect only in tumors and that exacerbation of toxicity or side effects of nanocarrier-encapsulated drugs may be minimal with this treatment.

Discussion

In the present study, we have tested a use of TβR-I inhibitor at a low dose to induce alteration in cancer-associated neovasculature to exhibit more leakiness for macromolecules, with less pericyte-coverage and greater endothelial area (Figs. 1 and 2). Because use of TβR-I inhibitor induced the same alteration in neovasculature in the Matrigel plug assay (M.R.K., unpublished data), a model of adult neoangiogenesis (23), the effects of use of TβR-I inhibitor on tumor vasculature observed in the present study may be common in adult neoangiogenesis. Although the roles of growth factors, including TGF-β, may differ during development and in adults, these phenotypes are reminiscent of those of knockout mice deficient in certain components of TGF-β signaling, e.g., endoglin (28, 29), ALK-1 (30, 31), and ALK-5 (32), in which loss of pericyte-coverage and dilatation of the vasculature in yolk sac or embryos were observed. These phenotypes are also consistent with the findings obtained on *in vitro* culture of endothelial cell lineages (33) and mesenchymal progenitor cells (34), which showed that pericyte maturation is promoted, and endothelial proliferation is inhibited, by TGF-β signaling. Vascular phenotypes due to defects in TGF-β signaling *in vivo* are also observed in two types of hereditary hemorrhagic telangiectasia (35, 36), which are induced by deficiencies of endoglin or ALK-1, which are components of TGF-β signaling in vascular endothelium. Because of inborn and life-long abnormality of TGF-β signaling in vasculature, these diseases result in a tendency toward hemorrhage in capillaries that is due to vulnerability of the vascular structure. These observations suggest that use of TβR-I inhibitor at a dose corresponding to that in mice in our study may have similar effects in humans. However, the inhibition of TGF-β signaling is only transient in our method, because of the use of small-molecule inhibitor, and the effects of TβR-I inhibitor may thus be far less severe than the phenotypes observed in hereditary hemorrhagic telangiectasia.

The changes in tumor neovasculature induced by TβR-I inhibitor resulted in enhanced extravasation of molecules, although in a molecular-size dependent manner. Accumulation of 2-MDa dextran with a 50-nm hydrodynamic diameter, Doxil with a 108-nm diameter, and micelle ADR with a 65-nm diameter was enhanced by TβR-I inhibitor in the present study, although accumulation of small-molecule agents, including ADR (MW 543.52) and BrdU (MW 307.10) (M.R.K., unpublished data), was not significantly enhanced. Dreher *et al.* (24) recently reported the molecular-size-dependency of intratumoral drug distribution, using a xenograft model of FaDu cells derived from human hypopharyngeal squamous cell carcinoma. They used several dextrans with molecular sizes ranging from 3.3 kDa to 2 MDa, with estimated hydrodynamic diameters of 3.5 nm to 50 nm, respectively. Dextran molecules of 3.3 kDa and 10 kDa, the smallest ones tested, were found to penetrate deeply and homogeneously into tumor tissue, although they remained in tumor tissue only transiently, for far less than 30 min. However, larger dextran of 2 MDa with a diameter of 50 nm, which we also used in the present study, for the most part remained in the vasculature in cancer tissue and reached only an ≈5-μm distance from the vessel wall at 30 min after injection. Although the histological characteristics of their model, which were not described in their report, may differ from those of the cancer models used in our study, the distribution of 2-MDa dextran observed by Dreher *et al.* agrees with that obtained without TβR-I inhibitor in the BxPC3 xenografts observed in the present study (Fig. 3). TβR-I inhibitor could thus enhance the accumulation of macromolecules with hydrodynamic diameters of >50 nm, common sizes for nanocarriers, in cancers other than those used in the present study. However, the range of sizes of macromolecules and histological patterns of cancer for which use of TβR-I inhibitor can exhibit enhancing effects remains to be determined.

In conclusion, we have proposed here a use of small-molecule TβR-I inhibitor at a low dose to enhance EPR effect in intractable solid cancers. This method could be a breakthrough in chemotherapy by using nanocarriers in these cancers. Because low-dose TβR-I inhibitor does not affect cancer cells, it may reduce the potential side effects of TGF-β inhibitors, and its enhancing effect is independent of the reactivity of cancer cells to TGF-β signaling. Use of TGF-β inhibitors may thus enable reduction of the systemic doses of nanocarriers and thereby decrease the adverse effects of anticancer drugs.

Methods

TGF-β Inhibitors, Anticancer Drugs, and Antibodies. TβR-I inhibitor was purchased from Calbiochem (San Diego, CA) (LY364947; catalog no. 616451). ADR was obtained from Nippon Kayaku (Tokyo, Japan) and purchased from Kyowa Hakko (Tokyo, Japan). Doxil was purchased from Alza (Mountain View, CA). Micelle ADR was prepared as reported (22) (see *SI Materials and Methods* for detailed information). The antibodies to PE-CAM-1 and VE-cadherin were from BD PharMingen (San Diego, CA), those to neuroglycan 2 and collagen IV were from Chemicon (Temecula, CA), and that to SMA was from Sigma–Aldrich (St. Louis, MO). The anti-phospho-Smad2 antibody was a gift from A. Moustakas and C.-H. Heldin (Ludwig Institute for Cancer Research, Uppsala, Sweden).

Cancer Cell Lines and Animals. BxPC3, MiaPaCa-2, and Panc-1 human pancreatic adenocarcinoma cell lines were obtained from the American Type Culture Collection (Manassas, VA). The OCUM-2MLN human diffuse-type gastric cancer cell line was previously established (27). BxPC3 cells were grown in RPMI medium 1640 supplemented with 10% FBS. MiaPaCa-2, Panc-1, and OCUM-2MLN cells were grown in DMEM with 10% FBS. BALB/c nude mice, 5–6 weeks of age, were obtained from CLEA Japan (Tokyo, Japan), Sankyo Laboratory (Tokyo, Japan), and Charles River Laboratories, (Tokyo, Japan). All animal experimental protocols were performed in accordance with the policies of the Animal Ethics Committee of the University of Tokyo.

Cancer Models. The effects of anticancer drugs were assessed by s.c. implantation of cancer cells into nude mice, and by orthotopic inoculation of OCUM-2MLN cells into the gastric walls of nude mice. A total of 5×10^6 cells in 100 μl of PBS for the xenograft models and the same number in 50 μl of PBS for the orthotopic model were injected into male nude mice and allowed to grow for 2–3 weeks to reach proliferative phase, before initiation of drug administration. For growth-curve studies, the day of initiation of drug administration was considered day 0, and TβR-I inhibitor, dissolved to 5 mg/ml in DMSO and diluted by 100 μl of PBS, or the vehicle control, was injected i.p. at 1 mg/kg on day 0 only in the experiment shown in Fig. 4*A* and on days 0, 2, 4, 6, and 8 in other experiments. Doxil, micelle ADR, and free ADR at 8 mg/kg, or normal saline as vehicle control, were also administered i.v. in 200 μl/vol via the tail vein on day 0 (Fig. 4*A*). In other experiments, micelle ADR at 16 mg/kg, free ADR at 8 mg/kg, or normal saline was also administered i.v. on days 0, 4, and 8. There were five mice per group per cell line. The doses of ADR and Doxil were determined based on the lethal doses in mice (22, 26). For biodistribution studies, three mice per group per cell line were treated with 8 mg/kg Doxil, micelle

ADR, or free ADR i.v., with and without TβR-I inhibitor at 1 mg/kg i.p. The mice were examined 24 h after injection.

Quantification in Tumor Models. Xenograft tumors were measured externally every second day until day 16, and tumor volume was approximated by using the equation vol = $(a \times b^2)/2$, where vol is volume, a the length of the major axis, and b is the length of the minor axis. Relative tumor volume was calculated by dividing tumor volume by that on day 0 (the day of initiation of treatment), where actual estimated volumes of xenografted tumors in mm^3 at initiation of drug administration were as follows (mean ± standard error): BxPC3 (in Fig. 4*A*), 76.4± 7.0; BxPC3 (in Fig. 4*B*), 74.4 ± 3.3; MiaPaCa-2, 221.2 ± 12.7; and Panc-1, 242.16 ± 24.5. For orthotopic OCUM-2MLN tumors, the area of the primary focus on the gastric wall was measured in Adobe Photoshop software, by opening the abdomen before initiation of treatment and at the end of the observation period. Relative tumor area was calculated by dividing tumor area by that on the day of initiation of treatment. The results were further analyzed statistically by the multivariate ANOVA test, using JMP6 software (SAS Institute, Raleigh, NC).

Histology and Immunohistochemistry. The excised samples were either directly frozen in dry-iced acetone for immunohistochemistry, or fixed overnight in 4% paraformaldehyde and then paraffin-embedded to prepare them for H&E or AZAN staining. Frozen samples were further sectioned at 10-μm thickness in a cryostat, briefly fixed with 10% formalin, and then incubated with primary and secondary antibodies. TOTO-3 for nuclear staining, Alexa488-, Alexa594-, and Alexa647-conjugated secondary antibodies, anti-rat and rabbit IgGs, Zenon labeling kit anti-rabbit and mouse IgG, and FITC-conjugated dextran (MW 2×10^6) were purchased from Invitrogen Molecular Probes (Eugene, OR). Samples were observed by using a Zeiss (Thornwood, NY) LSM510 Meta confocal microscope for immunohistochemistry, and an Olympus (Tokyo, Japan) AX80 microscope for H&E and AZAN staining.

Biodistribution. Xenografts were inoculated s.c. in nude mice and allowed to grow for 2–3 weeks before drug administration. We then injected TβR-I inhibitor at 1 mg/kg i.p. together with i.v. administration of Doxil, micelle ADR, or free ADR at 8 mg/kg. The tumors or organs were excised 24 h after injection of drugs, and frozen in dry-iced acetone to obtain fluorescence images or weighed and mixed with daunorubicin commensurate with the sample weight as an internal control and then frozen to prepare them for measurement by HPLC. The HPLC method used for analyses is described in ref. 22. To obtain fluorescence images, we performed cryostat sectioning of the frozen samples and washed the sections twice briefly with PBS but did not fix them to avoid elution of ADR. The samples were then observed with a Zeiss confocal microscope, using an excitation laser at 488 nm and a detection filter for the infrared region.

We thank Erik Johansson (University of Tokyo) for assistance. This work was supported by a Kakenhi (Grant-in-Aid for Scientific Research) in Priority Areas "New strategies for cancer therapy based on advancement of basic research" and the Project on the Materials Development for Innovative Nano-Drug Delivery Systems from the Ministry of Education, Culture, Sports, Science, and Technology of Japan. This work was also supported by the Foundation for Promotion of Cancer Research in Japan.

1. Muggia FM (2001) *Curr Oncol Rep* 3:156–162.
2. Ferrari M (2005) *Nat Rev Cancer* 5:161–171.
3. Hassan M, Little RF, Vogel A, Aleman K, Wyvill K, Yarchoan R, Gandjbakhche AH (2004) *Technol Cancer Res Treat* 3:451–457.
4. Emoto M, Udo T, Obama H, Eguchi F, Hachisuga T, Kawarabayashi T (1998) *Gynecol Oncol* 70:351–357.
5. Duncan R (2006) *Nat Rev Cancer* 6:688–701.
6. Kataoka K, Harada A, Nagasaki Y (2001) *Adv Drug Deliv Rev* 47:113–131.
7. Hamaguchi T, Matsumura Y, Suzuki M, Shimizu K, Goda R, Nakamura I, Nakatomi I, Yokoyama M, Kataoka K, Kakizoe T (2005) *Br J Cancer* 92:1240–1246.
8. Nishiyama N, Okazaki S, Cabral H, Miyamoto M, Kato Y, Sugiyama Y, Nishio K, Matsumura Y, Kataoka K (2003) *Cancer Res* 63:8977–8983.
9. MacKenzie MJ (2004) *Lancet Oncol* 5:541–549.
10. Fuchs CS, Mayer RJ (1995) *N Engl J Med* 333:32–41.
11. Burris HA, III, Moore MJ, Andersen J, Green MR, Rothenberg ML, Modiano MR, Cripps MC, Portenoy RK, Storniolo AM, Tarassoff P, *et al.* (1997) *J Clin Oncol* 15:2403–2413.
12. Watanabe N, Tsuji N, Tsuji Y, Sasaki H, Okamoto T, Akiyama S, Kobayashi D, Sato T, Yamauchi N, Niitsu Y (1996) *Pancreas* 13:395–400.
13. Matsumura Y, Maeda H (1986) *Cancer Res* 46:6387–6392.
14. Maeda H, Matsumura Y (1989) *Crit Rev Ther Drug Carrier Syst* 6:193–210.
15. Sofuni A, Iijima H, Moriyasu F, Nakayama D, Shimizu M, Nakamura K, Itokawa F, Itoi T (2005) *J Gastroenterol* 40:518–525.
16. Takahashi Y, Cleary KR, Mai M, Kitadai Y, Bucana CD, Ellis LM (1996) *Clin Cancer Res* 2:1679–1684.
17. Roberts AB, Wakefield LM (2003) *Proc Natl Acad Sci USA* 100:8621–8623.
18. Feng XH, Derynck R (2005) *Annu Rev Cell Dev Biol* 21:659–693.
19. Bandyopadhyay A, Agyin JK, Wang L, Tang Y, Lei X, Story BM, Cornell JE, Pollock BH, Mundy GR, Sun L-Z (2006) *Cancer Res* 66:6714–6721.
20. Yingling JM, Blanchard KL, Sawyer JS (2004) *Nat Rev Drug Discov* 3:1011–1022.
21. Sawyer JS, Anderson BD, Beight DW, Campbell RM, Jones ML, Herron DK, Lampe JW, McCowan JR, McMillen WT, Mort N, *et al.* (2003) *J Med Chem* 46:3953–3956.
22. Bae Y, Nishiyama N, Fukushima S, Koyama H, Matsumura Y, Kataoka K (2005) *Bioconjug Chem* 16:122–130.
23. Kano MR, Morishita Y, Iwata C, Iwasaka S, Watabe T, Ouchi Y, Miyazono K, Miyazawa K (2005) *J Cell Sci* 118:3759–3768.
24. Dreher MR, Liu W, Michelich CR, Dewhirst MW, Yuan F, Chilkoti A (2006) *J Natl Cancer Inst* 98:335–344.
25. McDonald DM, Choyke PL (2003) *Nat Med* 9:713–725.
26. Gabizon A, Tzemach D, Mak L, Bronstein M, Horowitz AT (2002) *J Drug Target* 10:539–548.
27. Yashiro M, Chung YS, Nishimura S, Inoue T, Sowa M (1996) *Clin Exp Metastasis* 14:43–54.
28. Li DY, Sorensen LK, Brooke BS, Urness LD, Davis EC, Taylor DG, Boak BB, Wendel DP (1999) *Science* 284:1534–1537.
29. Arthur HM, Ure J, Smith AJ, Renforth G, Wilson DI, Torsney E, Charlton R, Parums DV, Jowett T, Marchuk DA, *et al.* (2000) *Dev Biol* 217:42–53.
30. Oh SP, Seki T, Goss KA, Imamura T, Yi Y, Donahoe PK, Li L, Miyazono K, ten Dijke P, Kim S, *et al.* (2000) *Proc Natl Acad Sci USA* 97:2626–2631.
31. Urness LD, Sorensen LK, Li DY (2000) *Nat Genet* 26:328–331.
32. Larsson J, Goumans MJ, Sjostrand LJ, van Rooijen MA, Ward D, Leveen P, Xu X, ten Dijke P, Mummery CL, Karlsson S (2001) *EMBO J* 20:1663–1673.
33. Watabe T, Nishihara A, Mishima K, Yamashita J, Shimizu K, Miyazawa K, Nishikawa S-I, Miyazono K (2003) *J Cell Biol* 163:1303–1311.
34. Hirschi KK, Rohovsky SA, D'Amore PA (1998) *J Cell Biol* 141:805–814.
35. Lebrin F, Deckers M, Bertolino P, ten Dijke P (2005) *Cardiovasc Res* 65:599–608.
36. Fernandez-L A, Sanz-Rodriguez F, Blanco FJ, Bernabeu C, Botella LM (2006) *Clin Med Res* 4:66–78.

Available online at www.sciencedirect.com
ScienceDirect
International Journal of Pharmaceutics 346 (2008) 143–150
INTERNATIONAL JOURNAL OF PHARMACEUTICS
www.elsevier.com/locate/ijpharm

Pharmaceutical Nanotechnology

Effective anti-tumor activity of oxaliplatin encapsulated in transferrin–PEG-liposome

Ryo Suzuki [a,1], Tomoko Takizawa [a,1], Yasuhiro Kuwata [a], Mahito Mutoh [a], Nobuyuki Ishiguro [a], Naoki Utoguchi [a], Atsuko Shinohara [b], Masazumi Eriguchi [c], Hironobu Yanagie [c], Kazuo Maruyama [a,*]

[a] *Department of Biopharmaceutics, School of Pharmaceutical Sciences, Teikyo University, 1091-1 Suwarashi, Sagamiko, Sagamihara, Kanagawa 229-0195, Japan*
[b] *Department of Epidemiology and Environmental Health, Juntendo University School of Medicine, 2-1-1 Hongo, Bunkyo-ku, Tokyo 113-8421, Japan*
[c] *Department of Intellectual Property, Research Center for Advanced Science and Technology, The University of Tokyo, 4-6-1 Komaba, Meguro, Tokyo 153-8904, Japan*

Received 16 March 2007; received in revised form 10 May 2007; accepted 8 June 2007
Available online 16 June 2007

Abstract

Oxaliplatin (*trans*-L-diaminocyclohexane oxalatoplatinum, L-OHP) is a novel cisplatin derivative that can improve the side effects of cisplatin such as toxicity to the kidneys and peripheral nerve system. However, L-OHP is effective only when combined with 5-Fluorouracil (5-FU) and Leucovorin. The relatively low anti-tumor index of L-OHP alone is because low levels accumulate in tumor tissues due to high partitioning to erythrocytes *in vivo*. A successful outcome of cancer therapy using L-OHP requires the selective delivery of a relatively high concentration of the drug to tumors. The present study examines tumor-selective delivery of L-OHP using liposomes modified with transferrin-conjugated polyethyleneglycol (TF–PEG-liposomes). Delivery using these liposomes significantly reduced L-OHP partitioning to erythrocytes and improved the circulation time of L-OHP *in vivo*, resulting in enhanced extravasation of liposomes into tumors. The TF–PEG-liposomes maintained a high L-OHP concentration in tumors for over 72 h after intravenous injection, which was longer than that of the liposomes modified with PEG (PEG-liposomes). Intravenously administered L-OHP encapsulated within TF–PEG-liposomes (L-OHP: 5 mg/kg) suppressed tumor growth more effectively than PEG-liposomes, Bare-liposomes and free L-OHP. Although L-OHP is usually combined with 5-FU and Leucovorin, our results suggest that L-OHP encapsulated within TF–PEG-liposomes has potential for cancer therapy.

Keywords: Liposomes; Transferrin; Oxaliplatin; Targeting; Cancer therapy; Polyethyleneglycol (PEG)

1. Introduction

Surgery, radiotherapy and chemotherapy comprise the current choice of strategies used to fight cancer. However, the present range of anti-cancer drugs does not deliver satisfactory therapeutic effects due to many undesirable side effects.

Cisplatin (*cis*-diamminedichloroplatinum(II)) is one of the most effective agents against testicular, ovarian, head, neck and lung cancers. However, side effects include kidney toxicity, nausea, hearing impairment and irreversible peripheral nerve damage (Durant, 1980). To resolve these issues, considerable effort has been directed towards the development of cisplatin derivatives among which, oxaliplatin (*trans*-L-diaminocyclohexane oxalatoplatinum, L-OHP) has an anti-tumor effect against cisplatin-resistant murine leukemia cells (L1210 cells) (Kidani et al., 1980). L-OHP inhibits DNA synthesis by forming DNA adducts like cisplatin. In addition, it can also inhibit RNA synthesis unlike cisplatin (Tashiro et al., 1989). However, although L-OHP has no renal toxicity (Mathe

Abbreviations: CH, cholesterol; DSPC, distearoylphosphatidylcholine; DSPE, distearoylphosphatidylethanolamine; EPR, enhanced permeability and retention; L-OHP, *trans*-L-diaminocyclohexane oxalatoplatinum (oxaliplatin); MIP-MS, microwave-induced plasma mass spectrometer; PEG, polyethylene glycol; RES, reticuloendothelial system; TF, transferrin; TF–PEG-liposomes, transferrin-coupling pendant-type PEG-liposomes

* Corresponding author at: School of Pharmacy, Teikyo University, 1091-1 Suwarashi, Sagamiko, Sagamihara, Kanagawa 229-0195, Japan.
Tel.: +81 42 685 3722; fax: +81 42 685 3432.
E-mail address: maruyama@pharm.teikyo-u.ac.jp (K. Maruyama).
[1] These authors contributed equally to this work.

0378-5173/$ – see front matter © 2007 Elsevier B.V. All rights reserved.
doi:10.1016/j.ijpharm.2007.06.010

et al., 1989; Extra et al., 1990; Machover et al., 1996), its high incidence of adverse drug reactions including peripheral sensory neuropathy and thrombocytopenia remain clinically problematic (Extra et al., 1990). In the FOLFOX4 treatment together with 5-FU and Leucovorin (Rothenberg et al., 2003; Goldberg et al., 2004), L-OHP is a pivotal first line chemotherapeutic agent for treating colon cancer in over 60 countries.

A significant portion of L-OHP in whole blood is sequestered into erythrocytes (Pendyala and Creaven, 1993). The $T_{1/2}$ of L-OHP is 2.3 min (α-phase) and 49 min (β-phase) in mice, and 26 min (α-phase) and 38.7 h (β-phase) in humans. Free L-OHP in the blood is rapidly excreted by the kidneys resulting in the short α-phase, but the high partitioning of L-OHP to erythrocytes is reflected in the long β-phase. To induce the powerful anti-tumor effect of L-OHP, interaction with erythrocytes must be reduced, so that more L-OHP is delivered to tumors for internalization.

We recently described novel target-sensitive liposomes bearing polyethylene glycol (PEG), called pendant-type PEG immunoliposomes, in which antibodies or specific ligands are coupled to the extremities of surface-grafted PEG chains (Maruyama et al., 1995, 1997, 2004; Ishida et al., 2001; Iinuma et al., 2002; Hatakeyama et al., 2004; Kakudo et al., 2004; Miyajima et al., 2006). Functionalized PEG derivatives couple antibodies directly to the distal terminal of PEG chains incorporated in liposomes. We demonstrated that transferrin-coupling pendant-type PEG-liposomes (TF–PEG-liposomes) are effectively extravasated into solid Colon 26 tumors in mice, and internalized into tumor cells (Ishida et al., 2001). The residence time of TF–PEG-liposomes in the circulation is prolonged and reticulo-endothelial system (RES) uptake is low in tumor-bearing mice, resulting in enhanced extravasation of the liposomes into solid tumors. This phenomenon has been characterized as the tumor-selective enhanced permeability and retention (EPR) effect of macromolecules and lipidic particles including liposomes (Matsumura and Maeda, 1986; Ishida et al., 1999). Accumulation in solid tumors is due to the unique vascular characteristics of tumors such as hypervasculature and enhanced vascular permeability, as well as the absence of a lymphatic recovery system (Jain and Gerlowski, 1986; Dvorak et al., 1988). After reaching a tumor site, TF–PEG-liposomes are internalized by receptor-mediated endocytosis and are absorbed into endosome-like intracellular vesicles. The transferrin (TF) receptor concentration on tumor cells is considerably higher than that on normal cells (Wagner et al., 1994). TF receptor-mediated endocytosis is a normal physiological process through which TF delivers iron into cells (Huebers and Finch, 1987; Aisen, 1994). Therefore, the clearance of TF–PEG-liposomes from tumor tissue is so impaired that they remain in the tumor interstitium for prolonged periods (Ishida et al., 2001).

Since selective delivery and cell-entry mechanisms are features of TF–PEG-liposomes, the delivered species of liposome does not need natural affinity for the targeted tumor cells, thus rendering this system potentially applicable to a wide variety of effector molecules, including L-OHP. Here, we examined the potential of liposomes to selectively deliver therapeutic quantities of L-OHP to tumors. We prepared TF–PEG and PEG-liposomes encapsulating L-OHP and compared their tissue distribution in Colon 26 tumor-bearing mice with those of Bare-liposomes and free L-OHP. In addition, we examined the anti-tumor activities of TF–PEG-liposomes encapsulating L-OHP in mice bearing Colon 26 tumors.

2. Materials and methods

2.1. Animals and tumor cells

Six-week-old male BALB/c mice (Tokyo Experimental Animals, Inc., Tokyo, Japan) were maintained at the animal care facility of Teikyo University (Kanagawa, Japan) under a regulated period of light and provided with water and food ad libitum. Colon 26 cells, which are derived from a mouse colon carcinoma, were maintained in RPMI 1640 medium (Sigma–Aldrich Japan, Tokyo) containing 10% fetal calf serum (Gibco, Gaithersburg, MD) under a 5% CO_2 atmosphere at 37 °C.

2.2. Lipids and chemicals

Nippon Oil and Fats Co. (Tokyo, Japan) donated distearoylphosphatidylcholine (DSPC) (COATSOME MC-8080), distearoylphosphatidylethanolamine (DSPE) (COATSOME ME-8080), monomethoxy polyethyleneglycol succinimidyl succinate (PEG-OSu) and polyethyleneglycol bis(succinimidyl succinate) (PEG-2OSu). The number-average molecular weight of PEG(2K)-OSu and of PEG(3K)-2OSu was 2219 and 3230, respectively, and their polydispersity was 1.03 and 1.04, respectively, as measured using gel permeation chromatography. DSPE-PEG(2K) and DSPE-PEG(3K)-COOH were synthesized as described (Maruyama et al., 1995). Cholesterol (CH) and triethylamine were purchased from Wako Pure Chemicals (Osaka, Japan). Human iron-saturated TF was purchased from Sigma (St. Louis, MI) and L-OHP was donated by its developer, Dr. Y. Kidani (Kidani et al., 1980).

2.3. Liposome preparation

Bare-liposomes and PEG-liposomes were prepared from DSPC and CH (2:1, molar ratio) and DSPC, CH, DSPE-PEG(2K) (2:1:0.192, molar ratio), respectively. Small unilamellar vesicles (SUV) of the two types of liposomes were prepared using reverse-phase evaporation (REV). Lipids (300 mg) were dissolved in 4 ml of chloroform/diethyl ether (1:1, v/v) and then 2 ml of 8 mg/ml L-OHP in 9% (w/v) sucrose was dropped into the lipid mixture to form a w/o emulsion. The volume ratio of the aqueous to the organic phase was maintained at 1:2. The emulsion was sonicated for 1 min and then the organic phase was removed to form liposomes by evaporation in a rotary evaporator at 30 °C under vacuum for 1 h. The resulting liposome was extruded through a polycarbonate membrane (100 nm pore size) using an extruder device (Lipex Biomembranes Inc., Canada) maintained at 60 °C to obtain liposomes of a homogeneous size. Unencapsulated free L-OHP was removed by ultracentrifugation at 200,000 × g for 20 min at 4 °C (Hitachi CS120, S100AT5 rotor), and the pellets were resuspended in 9% sucrose.

We prepared TF–PEG-liposomes by coupling TF to PEG-liposomes as described (Ishida et al., 2001). Briefly, 1-ethyl-3-(3-dimethylaminopropyl) carbodiimide (EDC) and *N*-hydroxysulfosuccinimide (S-NHS) were mixed (DSPE-PEG(3K)-COOH:EDC:S-NHS = 0.067:2.5:6.3, mole ratio) with 1 ml of PEG-liposomes comprising DSPC, CH, DSPE-PEG(2K), DSPE-PEG(3K)-COOH (2:1:0.16:0.032, molar ratio) in MES buffer (10 mM MES in 150 mM NaCl, pH 5.5), and incubated for 10 min at room temperature. The mixture was eluted through a Sephadex G-25 column equilibrated with MES buffer (pH 5.5) and liposome fractions were collected. Various amounts of TF were added to the liposome fractions and gently stirred for 3 h at room temperature. The mixture was centrifuged at 200,000 × *g* for 20 min at 4 °C, and then the pellet resuspended in 9% sucrose was mixed with $FeCl_3$–nitrilotriacetic acid to yield diferric TF. This suspension was centrifuged at 200,000 × *g* for 20 min at 4 °C, and the precipitated TF–PEG-liposomes were resuspended in 9% sucrose. The lipid concentration was estimated using a phosphorus assay. Size of liposomes was measured using an electrophoretic light scattering spectrophotometer (ELS-700, Otsuka Electronics, Tokyo) and the L-OHP content was determined using a microwave-induced plasma mass spectrometer (MIP-MS, P-7000, Hitachi, Tokyo) as described below.

2.4. *In vitro cytotoxicity*

Colon 26 cells (5×10^3 cells/well) were seeded into 96-well microplates and cultured overnight. Samples were added to each well and the plates incubated for 4 h at 37 °C. The medium was removed and fresh medium was added to each well. After incubation for a further 2 days, cell viability was measured using the WST-1 assay (Cell counting kit, Wako Pure Chemicals, Osaka, Japan).

2.5. *Biodistribution in tumor-bearing mice*

Tumor-bearing mice were prepared by inoculating a suspension of Colon 26 cells (2×10^6 cells) s.c. into the backs of BALB/c mice. Biodistribution was investigated when the tumors ranged from 6 to 8 mm in diameter. L-OHP solution or L-OHP encapsulated within Bare-, PEG- or TF–PEG-liposomes was injected into the mice via the tail vein. At selected intervals thereafter, the mice were lightly anesthetized, bled via the retro-orbital sinus, then killed by cervical dislocation and dissected. The organs were excised and their L-OHP content was determined using a MIP-MS as described below. Total blood was assumed to comprise 7.3% of the body weight. Contamination with blood in the organs was corrected by examining the distribution of ^{51}Cr-labeled erythrocytes (Maruyama et al., 1993).

2.6. *Partitioning of* L-*OHP into erythrocytes*

Samples of blood collected in the presence of anticoagulant (sodium citrate) were centrifuged to obtain plasma and the precipitate containing erythrocytes (erythrocytes fraction). And concentrations of L-OHP were measured at various time points in whole blood, plasma and erythrocyte fraction using a MIP-MS as described below. Data were presented as the percentage of the total injected dose for each sample.

2.7. *Quantification of* L-*OHP*

Liposomes, whole blood, plasma, erythrocyte or tissue samples were digested using a programmed microwave procedure. Diluted liposome samples, 20–100 mg of wet tissue or 100 μl of plasma were weighed and placed in PFA vials (Taf-tainer vial, GL Science, Tokyo). Thereafter, 400 μl of concentrated nitric acid and 200 μl of hydrogen peroxide (Tama Pure AA 100, Tama Chemicals, Tokyo) were added and digestion proceeded in a microwave oven (MLS-1200 MEGA; Milestone s.r.l., Italy) as follows; 250 W for 5 min, 0 W for 1 min, 250 W for 5 min, 400 W for 5 min, and 600 W for 5 min. The digested samples were brought to 1.0 ml with milli Q water, and then diluted. The content of L-OHP was measured using a MIP-MS. Europium (Eu) was added to the assay mixture and calibration standards at 0.1% and 20 ng/ml (final concentrations), respectively. The L-OHP concentrations were calculated from ion counts at platinum (Pt) using the calibration method with internal standard correction. The L-OHP concentrations in tissues were expressed as micrograms of L-OHP per gram tissue.

2.8. *Measurement of serum albumin, total protein, glutamic–oxaloacetic transaminase (GOT), glutamic–pyruvic transaminase (GPT) and blood urea nitrogen (BUN)*

A solution of L-OHP or L-OHP encapsulated within Bare-, PEG- or TF–PEG-liposomes was injected into tumor-bearing mice via the tail vein at a dose of 5 mg L-OHP/kg. Three days later, the mice were anesthetized and blood samples were collected using glass capillaries from the vein of the fundus oculi. Serum obtained from blood samples by centrifugation was tested for albumin, total protein, GOT, GPT and BUN using respective kits (A/G B test Wako for albumin and total protein, GOT-UV Test Wako for GOT, GPT-UV Test Wako for GPT and Urea Nitrogen B Test Wako for BUN, Wako Pure Chemicals, Osaka, Japan).

2.9. *Therapeutic effects of* L-*OHP encapsulated liposomes*

A suspension of Colon 26 cells (2×10^6 cells) was inoculated s.c. into the backs of BALB/c mice. Therapeutic effects were examined when the tumors ranged from 8 to 10 mm in diameter. A solution of L-OHP or L-OHP encapsulated within Bare-, PEG- or TF–PEG-liposomes was injected twice into the tumor-bearing mice via the tail vein at a dose of 5 mg L-OHP/kg on days 9 and 12 after tumor cell inoculation. The two perpendicular diameters of tumors were obtained at intervals of a few days using a slide caliper and then tumor volumes were calculated using the formula 0.5 ($A \times B^2$), where A and B are the longest and shortest dimensions (mm) of the tumor, respectively. Tumor growth ratio was represented as the ratio for the tumor